LUND UNIVERSITY

Master Thesis
Division of Solid State Physics
Department of Physics
Faculty of Engineering, LTH
June 2016

Electro-optical characterization of NanoWire Solarcells

Author:

Ida Ångbäck
Phone: +46 (0)709984619
E-mail: tfy11ian@student.lu.se

Supervisors:

Dan Hessman, Associate Professor (Main Supervisor)
Magnus Borgström, Professor
Solid State Physics, Lund University

Examiner:

Carina Fasth, Associate Professor
Solid State Physics, Lund University

Abstract

A sample with five Nanowire Solar Cell (NWSC) devices of equal design were performance evaluated by characterizing the current spatially and by investigating the angular and polarization dependence.

For spatial characterization a Scanning Photocurrent Microscopy (SPCM) setup was developed using a highly focused laser which is scanned across the device as the photocurrent is measured. The photocurrent image (PCI) was complemented with simultaneous reflection detection. A reflection image (RI) could give further information about the investigated device. Images revealed high quality devices with high currents and little defects. The technique resolved features down to single nanowire scale with highest resolution of 0.55-1 µm according to an empirically found laser spot size.

Defects, characterized comparing PCI and RI revealed spots of missing nanowires (NWs), scratches of defected/missing NWs, large surface artifacts and dirt particles attached to the surface. These originate from different steps in the processing and information from other characterization techniques, such as scanning electron micrsocopy (SEM), is needed to conclude the origin and indicate how to avoid them.

A setup for investigating the angular and polarization dependence of the photocurrent was developed using a broad band light source and Fourier Transform Spectrometer. Results for the total spectrum show similar angular dependence as for planar solar cell devices but vary strongly with energy, a feature that distinguished NWSCs from planar devices. The angular dependence was the lowest for 900 nm and highest at 800-700 nm.

The polarization dependence was measured in the same manner for different linear polarizations. Results for different polarizations show different angular dependence varying with energy. The maximum intensity difference between the polarizations, the Brewster angle, varied between 60° and 80° for different energies. This is a larger variation than for planar InP where the same wavelength range corresponds to Brewster angles of 74°-78°.

Acknowledgements

I would like to thank all who have helped me throughout the work of my thesis. Special thanks to:

Dan Hessman, my main supervisor who has helped me all the way through my work - Thanks for your thorough explanations and for all the interesting discussion we have had.

Magnus Borgström, for his guidance and help with detailed NWSC questions

Nicklas Anttu, for his simulations of polarization dependence and help with theoretical questions

Vishal who so kindly helped me bonding the sample

Shishr for being a considerate and motivating lab partner

My family, friends and colleagues for their support

And last but not least, thanks to The Division of Solid State Physics for giving me the opportunity to join you for 6 months, for all the inspiring presentations and for every delicious Friday fika.

Table of Contents

1. Introduction

1.1. Background

With the growing need for renewable energies there has been an increased interest for solar energy which is now a rapidly expanding field [1]. In order to make solar energy and solar panels more attractive and to allow for wide implementation, a better cost-to-efficiency ratio is needed. The most commonly used solar cell technique is the single-junction silicon solar cell. This type of solar cell has, in relation to other solar cell techniques, a high efficiency in combination with low cost. The efficiency of such silicon solar cells has today reached 25.6% and is still being increased by better material purification and new techniques [2] [3] [4]. Such solar cells are getting close to the Shockley-Queisser limit (the theoretical maximum efficiency limit) which for a silicon single junction cell is 30% [5]. Another solar cell technique with higher Shockley Queisser limit is the hetero-structure multi-junction solar cell. This has today reached an efficiency of 38.8% for a five junction cell [2]. Multijunction cells however, have a very high cost due to expensive material usage [6]. In order to decrease the cost-to-efficiency ratio of solar cells both parameters need to be addressed. Nanowire implemented solar cells are one way of doing this. Nanowires show advantages in all parts of the light absorption process due to their light trapping geometry. They can allow for new material combinations and specially designed multi-junction structures [6]. As a result of the lower volume fill factor (compared to planar devices) the cost may be reduced by reduced material usage.

1.2. Motivation

Investigations of nanowire solar cells (NWSCs) for identification of manufacturing defects and possibilities for design improvements are needed to further improve their performance. To optimize material usage and increase efficiency it is crucial that defects are minimized. The first step in achieving this is to identify and characterize the defects. This can be realized by spatially mapping the photocurrent of the NWSC.

The spatially resolved photocurrent may then be compared to optical images of the device structure and one could identify what type of defects that affect the induced photocurrent. Such defects could be scratches, missing nanowires, irregularities in the coating and dirt or dust attached to the device. These defects and patches of low induced photocurrent may either be results from undesired effects in the manufacturing process or undesired effects of the actual device design. The information could consequently be used to improve the NWSC manufacturing process by removing steps that generate defects, introducing steps that reduce them or by changing the design.

Incidence angle and polarization of incident radiation are important parameters to look into in order to get a greater understanding of the NWSC and of how it would perform under actual operating conditions. To meet such conditions and to find the ideal NWSC design the influence of these parameters on the photocurrent must be established both through simulations and experimental testing.

1.3. Objectives

The work in this thesis investigates the NWSC using two different setups. The goal of the work is to attain measurement results that address the issues presented in section 1.2. The work is divided into two main objectives.

1. The first objective aims to use and further develop a laser characterization technique, already proven to give successful measurements, in order to spatially examine the photocurrent in NWSC. Through this technique we want to be able to look at the performance at local parts of the NWSC. This way the absorption and the effect of manufacturing defects could be investigated at a microscopic scale. The information could then be compared to already existing information about the NWSC at macroscopic scale.
2. The second objective is to investigate two particular aspects of the incoming light, namely incidence angle and light polarization, and their effect on the NWSC's performance. These light properties will inevitably have an impact on the NWSC's efficiency and this thesis aims to give a greater understanding of the nature of this impact.

Information about the correlation between the NWSC performance and the manufacturing defects, angle of light and polarization of light may be an input as to how both the design and the manufacturing procedures of the NWSC can be improved.

1.4. Thesis Outline

This thesis presents the work with the spatial photocurrent microscopy (SPCM) and angular/polarization dependence investigation that has been carried out during this project. The report starts by giving an introduction to the basic principles of solar cells and NWSCs before getting into these two topics. The introduction is followed by a description of the SPCM technique and of the setup development process. Measurements that were made are then explained and results are presented and discussed. The SPCMs is analyzed in terms of performance, defects and correlation to a characterization made by Sol Voltaics' (producers of the NWSC).

Next, theory behind angular dependence for solar cells is presented, the measurement setup is described and measurement results are presented and discussed in comparison to the theory. Lastly polarization dependence is described in theory together with a simulation. The measurements are described and results obtained are discussed.

Conclusively important results are summarized, parallels are drawn between the results from the different measurement setups and possible setup improvements and interesting features for future investigations are suggested.

2. Introduction to Photovoltaics

A solar cell is in principle a simple semiconductor device. It can be made from single crystal, crystalline or amorphous semiconductors [7]. Today several different solar cell designs exist. For simplicity a crystalline single junction solar cell will be used as example to introduce the operating principles of a solar cell.

When a semiconductor is illuminated, photons with high enough energy will be absorbed and generate electron-hole pairs. The electrons and holes are then free to move in the structure but will recombine whenever they come too close to each other. If they experience an electric field however, they will drift in opposite directions and may be collected in an external circuit. Consequently there will be a so called photocurrent flowing in the semiconductor. In solar cells the electric field is created at the intersection between two materials of different charge carrier concentrations. To collect the drifting charge carriers both sides of the solar cell are connected to electrodes and the cell serves as a battery [7].

2.1. Pn-junction

The intersection mentioned is called a pn-junction. This is the junction between two semiconductor materials that are said to be p- and n-doped. To the n-doped material atoms called donors have been added which add electrons to the material. Atoms called acceptors have been integrated in the p-doped material. These collect free electrons and result in a material with deficiency of electrons, usually thought of as an excess of positively charged holes.

A pn-junction is created when an n-type material is joined with a p-type one [8]. Free carriers will then start to diffuse (movement driven by the difference in charge carrier concentration); electrons in the n-type material diffuse into the p-type material and holes in the p-type material diffuse into the n-type material. See Figure 1.

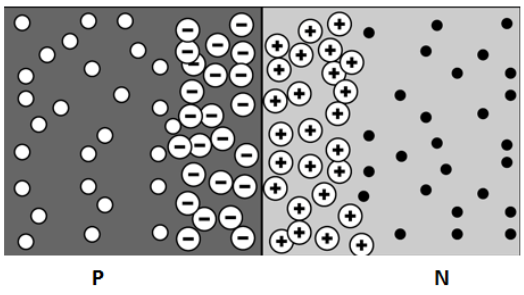

Figure 1: Illustration of a pn-junction. White circles represent holes, negative circles ionized (negatively charged) acceptors, positive circles ionized (positively charged) donors and black circles electrons. (Modified figure [9])

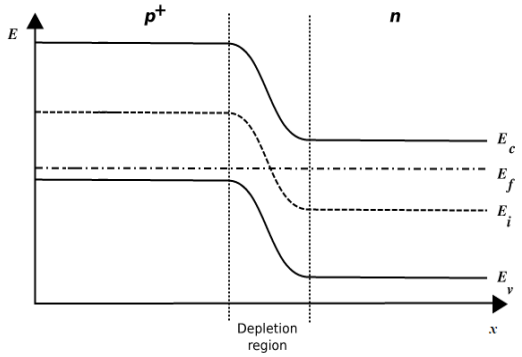

Figure 2: Band structure for p and n materials with corresponding energy levels (left) and band structure for pn-junction with resulting fermi level and depletion region (right). (Modified figure [10])

After a while steady state is reached where the diffusion of carriers is held back by an electric field that is created at the junction. The bands structure of the pn-junction can be illustrated as in Figure 2.

2.1.1. Pn-junction under illumination

When the pn-junction is subject to incident radiation this radiation may create electron-hole pairs that will be separated by the built-in electric field. The generated charge carriers, that start drifting in opposite directions, are what give rise to the photocurrent, light induced current [11].

2.1.2. Quantum efficiency

Quantum efficiency is a measure of how efficiently the solar cell collects incoming photons [12]. This is the ratio between the number of carriers that are collected and the amount of photons incident on the cell. External quantum efficiency (EQE) refers the ratio of collected carriers to the number of photons incident on the cell. The internal quantum efficiency (IQE) accounts for optical losses due to transmission and reflection. This is the ratio of collected carriers to the number of photons that have actually been absorbed by the cell without being transmitted or reflected away. The IQE can be found from the EQE by measuring the current together with reflection and transmission of the device.

The quantum efficiency varies with energy of incoming light. In solar cells factors such as reflection, transmission and recombination effects may reduce the value [13]. The absorption and diffusion lengths affect the probability of charge carriers to be collected and thus affect both EQE and IQE.

2.1.3. Photovoltaic effect

We have now discussed the photocurrent generated in solar cells. For the cells to be useful they need to generate power. This means that both a current and a voltage have to be present and the power will be given as the product of the two.

If the device is connected to an external load there will be a built up charge at the p- and n-side which creates a new electric field in the opposite direction to the built-in one [14]. This process is called the photovoltaic effect and the induced electric field gives rise to a voltage across the solar cell; the solar cell generates power.

2.1.4. Maximum power and efficiency

Solar cells are operated at active operating points which means that they are connected to a load in order to generate maximum power output [15]. The power delivered is given by the product of the net current and net voltage. The power is the area under the inverted IV-curve, Figure 3, where the maximum power point is the point on the curve that induces the maximum achievable power. A solar cell array is ideally operated around this point.

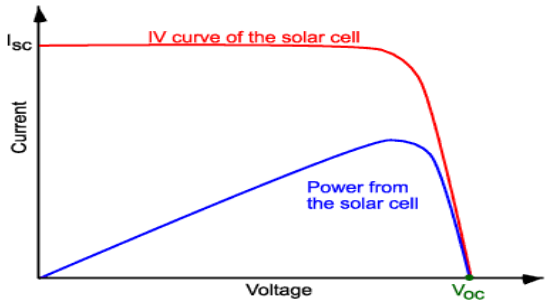

Figure 3: Typical inverted IV-curve for a solar cell (red) and corresponding power (blue). (Original figure [16])

Maximum power, P_m delivered is given by:

$$P_m = V_m I_m$$

Where V_m and I_m is the voltage and current at maximum power point. A parameter that is often used is the fill factor, FF, defined as the ratio between the maximum power and the short circuit current, I_{sc}, times open circuit voltage, V_{oc}:

$$FF = \frac{I_m V_m}{I_{sc} V_{oc}}$$

The efficiency, η, is the ratio between the maximum power and the power of the incoming light. Using the FF the efficiency is expressed as:

$$\eta = \frac{I_{sc} V_{oc} FF}{P_s}$$

Where P_s is the power of the incoming light.

[17]

2.1.5. Photovoltaic single junction Solar cell

A photovoltaic (PV) single junction solar cell consists of a shallow pn-junction on the surface of the solar cell, illustrated in Figure 4 [8]. On top of the surface there is an electrical contact (usually with fingers spreading out over the surface) and the entire back of the device is covered with a second electrical contact. To maximize the illumination entering the device there is usually an antireflection coating on the top surface.

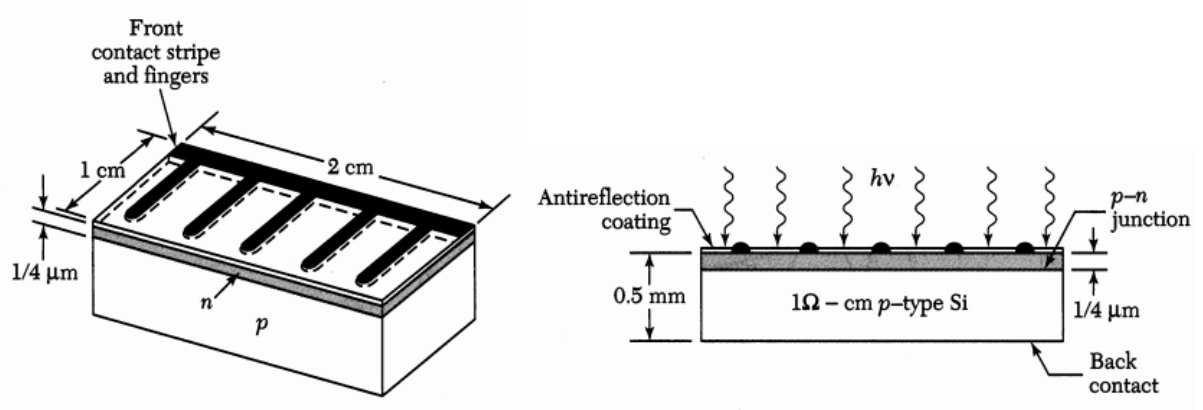

Figure 4: Illustration of a single junction solar cell. (Modified image [8])

2. Nanowire Solar cells

The physics of NWSCs is rather complex and covers physical principles that are still being investigated. The following section is an attempt to give an explanation of the main properties of nanowires that are relevant to the NWSC application. It will also give a brief explanation of the nanowire growth and nanowire solar cell production together with a presentation of the devices investigated in this project.

2.1. Structure

There are different NWSC structures. The most common are the nanowires with p-n junction in either radial or axial orientation, illustrated in Figure 5.

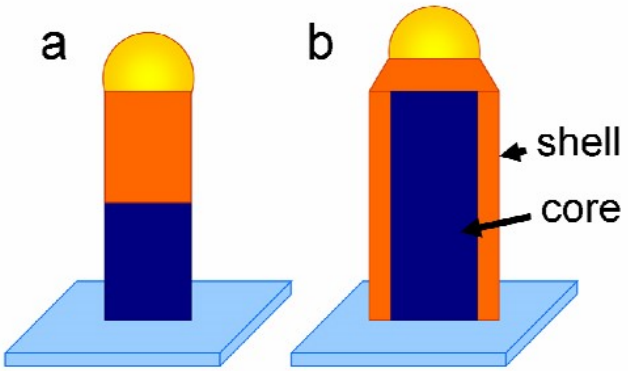

Figure 5: Illustration of a) nanowire with axial pn-junction and b) nanowire with radial pn-junction. (Original image [18])

The nanowires investigated in this thesis have the axially defined structure. The advantage of this design is that it fully benefits from the unique heterostructure freedom that allows new material combinations [6].

2.2. Properties

The use of nanowires may decrease the reflectance of the solar cell surface which is favorable for the solar cell performance and efficiency [19]. The reflectance shows a decrease of one to two orders of magnitude over the full spectrum for silicon NWSCs compared to silicon thin film cells of the same material use.

Nanowires also show potential of increasing light trapping by giving strong light trapping effects [20]. It has been shown that a Si nanowire array increases the path length that a photon travels before being absorbed or transmitted as compared to that of thin Si films. This increases the chance for the photon of being absorbed. For radial silicon NWSC the path length of incident solar radiation was shown to increase by a factor of 73% compared to the thin film cell of same thickness. This makes the use of nanowires superior to other light trapping methods.

The light trapping effect gives the nanowire a very high light absorption [19]. For a standing single nanowire on silicon substrate the light absorption was enhanced by a factor of 10-70% compared to an equivalent (in material usage) thin film solar cell when the diameter was varied. This can also be described by their absorption cross section which is the cross section within which the nanowires

absorb light. This is often, in the nanowire case, larger than the physical size of the nanowire. To absorb photons from an area outside of the nanowire corresponds to a built-in light concentrator and is a key factor in yielding the high light absorption. A light concentrator also has another benefit; it increases the open-circuit voltage which leads to increased power and increased efficiency.

Solar cells with nanowires are expected to generate similar currents to those achieved with planar cells but for a lower volume fill factor [21]. It is still unclear if the NWSC will exceed the efficiency limit of planar solar cells but their built-in light concentration and absorption indicate that it should be possible. Additionally they ease the requirements to achieve similar efficiencies and give opportunity for lower costs by enabling use of different materials, material combinations, new processing steps and, as mentioned, lower fill factor.

2.3. Processing

Nanowires that are composed of a mix of materials from group III and group V in the periodic table (such as InP) are particularly promising for electronics and optoelectronics applications [18]. They have advantageous properties such as high electron mobility, direct band gap and high quantum efficiency. In order to develop successful nanowire devices the fabrication process has to be well controlled to achieve the right shape, composition, purity, crystal structure and optical characteristics.

Bottom-up process

A technique that is usually implemented for nanowire fabrication is Metalorganic Chemical-Vapor deposition (MOVPE) [18]. This is a flexible and well-controlled way of growing nanowires. A gold particle is deposited on the substrate. The nanowires will then grow through a bottom-up process underneath the gold particles; illustration is shown in Figure 6.

1. A nanoimprint technique (practically a stamp) together with metal evaporation is used to form the gold seed particles in arrays on the substrate. The processing step is finished by lift-off of the imprint [21]. (figure() a),b))
2. To initiate the growth precursors of III and V species in vapor phase are supplied to the substrate at a given temperature. The gold particle then mixes with the group III species particle and forms a liquid or solid alloy. This corresponds to the growth of nanowires and the process time sets their length [18]. (figure() c),d)) The p- and n-dopants are introduced in this step giving rise to the axial pn-juntion (illustrated in Figure 5) [22].
3. As the nanowires are ready the metal seed particles are removed by wet etch to reduce reflection from the metal.
4. Sputter deposition of a transparent conducting oxide layer made of indium tin oxide (ITO).
5. The contact pads are deposited by thermal evaporation and UV lithography is carried out to define the cell and the metal contact pads [21] .

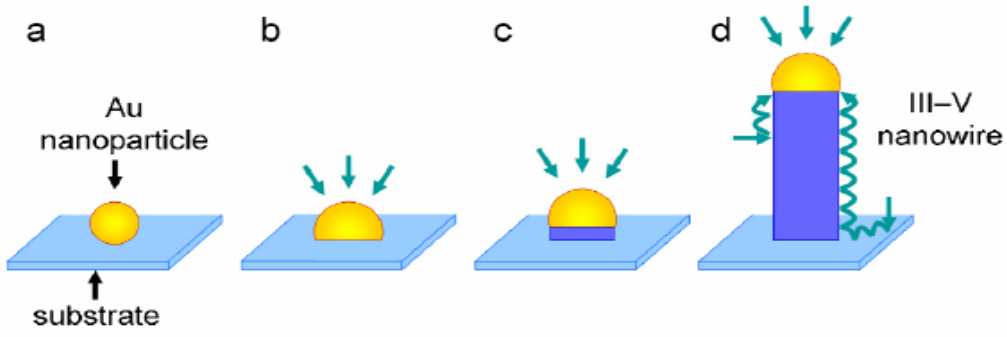

Figure 6: Illustration of growth of III-V compound nanowires using MOVPE; a) Gold nanoparticles are deposited onto substrate. b) They form an Au-group III alloy as growth precursors of group III materials are supplied in vapor at given temperature. c) Deposition continues with III-V material at interface between nanoparticle and substrate leading to nanowire growth underneath gold particle. d) Further nanowire growth, arrows indicating absorption and diffusion of the reaction species that contribute to growth. (Original Image [18])

2.4. Sample information

The solar cell mainly tested in this thesis was an InP nanowire solar cell with the pn-juntion in the axial direction. The nanowires stand on the substrate as illustrated in Figure 8. The geometry of the wires is 200 nm in diameter, 1.2 µm in length and nanowire pitch of 500 nm (hexagonal pattern). The growing process of these wires mainly follows the one described in section 2.3 with the difference that in step 4 benzocyclobutene is deposited as a filling material between the nanowires. This results in a rather planar surface of the NWSC.

When the experimental setup was completed the NWSC described was to be prepared for measurements. The sample was electrically bonded resulting in 5 successful connections to device B, D, F, H and J shown in Figure 7. The bonding of device F unfortunately came off after one successful measurement and no further signal was received from the device.

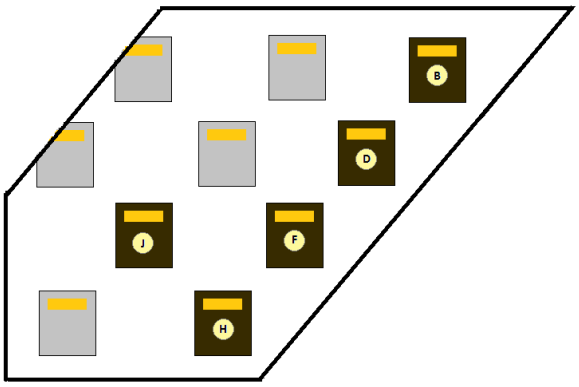

Figure 7: Illustration of solar cell devices on the new solar cell sample. Dark cells (called B, D, F, H and J) indicate successfully bonded cells (although F would show to be unreliable).

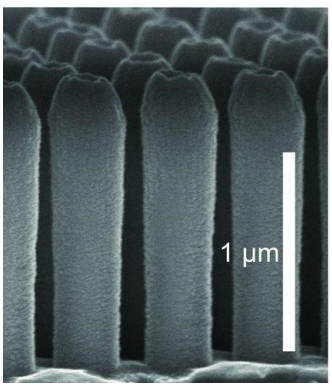

Figure 8: An image showing the nanowires as they stand on the solar cell. Image gained through scanning electron microscopy. (Modified image [21])

4. Spatial photocurrent microscopy

This chapter covers the work with the spatial photocurrent mapping. The technique is explained, the process of building the setup is presented and lastly the results are shown and discussed.

4.1. Scanning technique

The spatially resolved photocurrent of the NWSCs is mapped using scanning photocurrent microscopy (SPCM). The excitation source is a highly focused laser beam that is scanned over the device while measuring the generated short circuit current.

To get a complete understanding of the complex details of the properties of nanowire devices a combination of several characterization techniques is needed [23]. The parameters (measured or calculated) that are commonly used to characterize the NWSC are short circuit current, open circuit voltage and efficiency. Commonly this is done using a solar simulator at 1.5AM.

SPCM can be used as a complementing characterizing technique and has been used in several studies to characterize the photocurrent in solar cell devices, single nanowires and nanowire devices. This has emerged as a versatile technique to evaluate the electrical properties of nanowires [23]. The SPCM may also increase understanding of nanowire devices as it is compared to information obtained by scanning electron microscopy (SEM), atomic force microscopy and Kelvin probe force microscopy [24] [25].

4.1.1 Resolution

The resolution in images obtained with this technique will be highly governed by the laser spot size. For conventional imaging, through circular apertures and lenses, the limit to the resolution (diffraction limited) is defined by the Rayleigh criterion. Other definitions exist, differing in the definitions of when a feature is resolvable.

Two points imaged through a circular aperture will be resolvable until they reach a minimum distance between each other. This minimum distance is set by the Rayleigh criterion. The light waves from the point sources will diffract as they pass through the aperture and give rise to an Airy pattern at the image plane. According to the Rayleigh criterion the minimum distance between the points is when the maximum of the Airy disk for one point coincides with the first minimum of the other. The intensity pattern is governed by the first order Bessel function and gives an Airy disk radius, r, of:

$$r = \frac{1.22\lambda d}{D}$$

Where λ is the wavelength of the light source, d is the distance to the image plane and D is the diameter of the aperture. When focused through a lens (d = focal length) this can be expressed with the numerical aperture, NA as:

$$r = \frac{1.22\lambda}{2NA} = \frac{0.61\lambda}{NA}$$

Laser beams are usually described by Gaussian beams and do not have a "square" intensity distribution and sharp edges. Therefor the limit *r* is a suitable approximation as long as the aperture of the microscope objective is overfilled by the laser beam. This way the beam can be approximated

by a plane wave which is the assumption made in the derivation of the Rayleigh criterion. For the laser wavelength of 532 nm and NA of 0.8 used in this thesis the resolution limit is $r \approx 405\ nm$.

The SPCM technique is carried out by scanning a laser and detecting the induced photocurrent along the sweep. The smallest feature that will be resolvable will depend on the size of the laser spot that hits the NWSC surface but also on the induced photocurrent. The fact that the nanowires interact with the light and have larger cross sections than their physical area may affect the resolution. During the discussion of the results (section 4.4.2) the resolution will be empirically investigated by estimating the smallest feature observable. This way both the laser spot size and the nanowire-light interaction are taken into account. The resolution limit for laser beams is usually multiplied by a quality factor M^2 which describes how well the beam matches the ideal one. In this setup it might be suiting to introduce a similar factor for matching the empirically found resolution value with the theoretical one. This would be an indicator as to how ideally the setup is aligned.

To increase the details that a laser scanning technique may resolve a few parameters should be considered. The limit as described above sets an estimation of the size of the smallest resolvable feature. To increase accuracy and reduce the noise on the other hand a high scan density needs to be used [26]. Thus, the higher the spatial frequency in measuring points the higher the accuracy and noise reduction.

This implies that a high resolution imaging can be obtained if measurement points (pixels) along the line are taken with spacing smaller than the spot size. The maximum amount of pixels that may be taken along a scanning line will be governed by the maximum frequency at which the measurement setup can measure, detect and store a measurement value. Factors influencing this are speed in computer communication and detector and maximum speed of the translation stage.

4.1.2 Studies of solar cells and nanowire devices using SPCM

A previous study used SPCM for scanning of a microwire solar cell (in contrast to NWSC) [27]. This was done in order to analyze different designs and their corresponding ability to genera te photocurrent. Hence their intention using SPCM was similar to the one of this thesis but applied at a larger scale. The microwires on the array had a diameter of 2-3 micrometers, standing on a 7 micrometer pitch and their scanning was performed by a 650 nm laser with a beam waist of around 1 micrometer leaving the photocurrent from individual microwires to be resolvable. In the SPCM scans from this study the influence of single wires and single missing wires can easily be seen as bright and dark spots respectively. The current was maximized when the illumination was centered on a microwire and minimized when illumination was centered between 4 adjacent wires.

One can draw the conclusion that to see the influence of individual microwires the spot size used in this study (beam waist at the scale of 1 μm) is small enough. For the NWSC used in this thesis however, with nanowires standing in 500 nm pitches, a spot size on the 500 nm scale is needed, thus making a single nanowire resolution a greater challenge. This challenge has been overcome in a study that investigates the photocurrent in Patterned Radial GaAs Nanopillar Solar Cells [28]. The SPCM was executed with a 544nm laser at diffraction limited resolution. The short circuit current was measured as the laser swept over the device with a spot size of 300 nm determined from full-width at the intensity of $1/e^2$. The SPCM scanning of the devices in this study showed clear regions with high and low current alternating in correspondence to the nanowire array and the spacing between them. It was noticed that the current between the nanowires was non-zero. This could according to

the authors be explained by the relation between laser spot size and nanowire spacing. The nanowire diameter was 320 nm and the spacing of the nanowire stamp was 600nm. The laser having a spot size of 300 nm, slightly larger than the resulting distance between single nanowires, could explain the nonzero current seen in between the nanowires.

Spectrally resolved SPCM was recently used in a study (2013 [24]) on nanowire solar cells to successfully characterize the photocurrent and spectrally resolve the EQE. The study uses several techniques to get a greater picture of the NWSC properties. The authors correlated the SPCM information with information of structure and composition obtained by AFM and SEM. The nanowires in the investigated solar arrays were GaN nanowires standing in 500 nm pitches (in a hexagonal pattern). This study concluded that the SPCM method can be a useful method to spatially characterize new NWSC designs and architectures. The study performed scans with 405 nm laser and a 500 nm laser. Figure 9 shows one of their scans where the photocurrent is clearly spatially resolved. One can also see that the scan provides information about how the array performs for different regions. The spot size for the 405 nm and the 500 nm laser was 550 nm and 680 nm respectively. This corresponded to diffraction limits of 275 nm and 340 nm. The 500 nm laser gives similar difference between diffraction limit and nanowire pitch as for the laser and nanowire array used in this thesis which indicates that promising results can be expected.

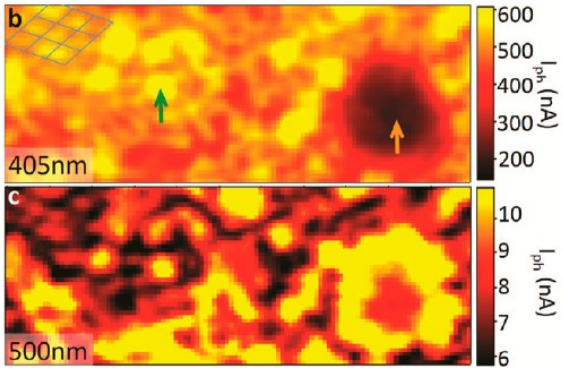

Figure 9: An 11x4.3 µm scan of a GaN–InGaN core–shell nanowire array device using SPCM with a 405nm laser (top) and a 500nm laser (bottom). The grid identifies a nanowire array region. The authors define different type of regions namely, dark regions of low height (green arrow) and bright regions of elevated height (yellow arrow). (Modified image [24]

A different study used SPCM to correlate information obtained with Kelvin probe force microscopy to investigate a single axial GaAs nanowire pn-diode [25]. These techniques enabled them to visualize the axial doping modulation, to determine the extension of the depletion region and to localize the position of maximal photo response in the single nanowire pn-junction. The latter was made using the SPCM in order to estimate the potential of the device in solar cell applications. They were able to establish that high photocurrent was induced in the region of the pn-junction but no photocurrent was detected in the areas close to the contacts or in the p- and n-regions, as is desired for the photodiode. In contrast to studies mentioned earlier in this chapter, this SPCM scan was made along the single nanowires as opposed to scanning from the top across a nanowire array. Nevertheless this proves the potential of SPCM for characterization of the photo response in nanowires.

4.2. Measurement setup

The final setup is illustrated in Figure 10. This is composed of a 532 nm laser that is directed through a microscope onto the sample/sample holder. Connected to the microscope is a camera, for overview of the sample. The sample holder sits on a translation stage that moves in the plane perpendicular to the laser beam. A photodiode is placed at one of the microscope oculars for detection of reflected laser light. Two lock-in amplifiers, connected to the sample and the photodiode respectively, are connected to a computer where a custom-made computer program is used to receive and read out information and to run the scan.

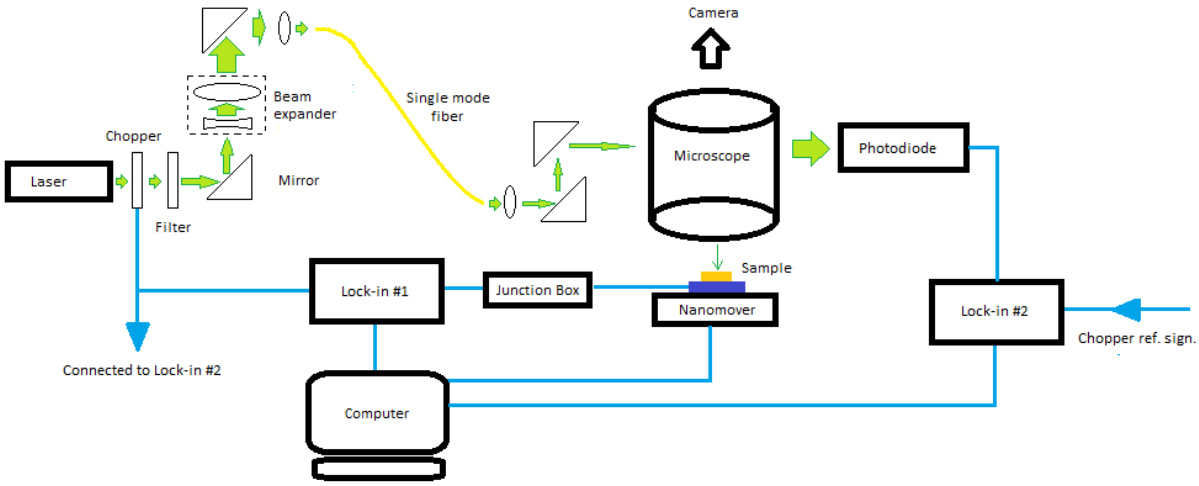

Figure 10: An illustration of the final setup for spatial photocurrent mapping. The laser is coupled to a single mode fiber (by mirrors and beam expander). At the output of the fiber the laser is sent into the microscope and focused down to hit the sample. Induced current is detected by a lock-in amplifier. Reflected laser light is detected by photodetector and measured with a second lock-in amplifier.

4.2.1 Setup development process

4.2.1.1 Initial Setup

The setup that was initially used in the lab is illustrated in Figure 11. This can be seen as a beginning of the setup that was to be constructed in this thesis and had been made by a previous thesis student. The setup was to be further developed in order to accomplish spatially resolved photocurrent measurements. As seen in the figure the initial setup included a laser source which was focused into a multimode fiber. The multimode fiber guided the light to an optical microscope (into which the beam was directed using mirrors). The microscope then had a beam pass through for the laser, a lamp for sample monitoring and a connected camera shown on a TV-screen to facilitate in vivo monitoring.

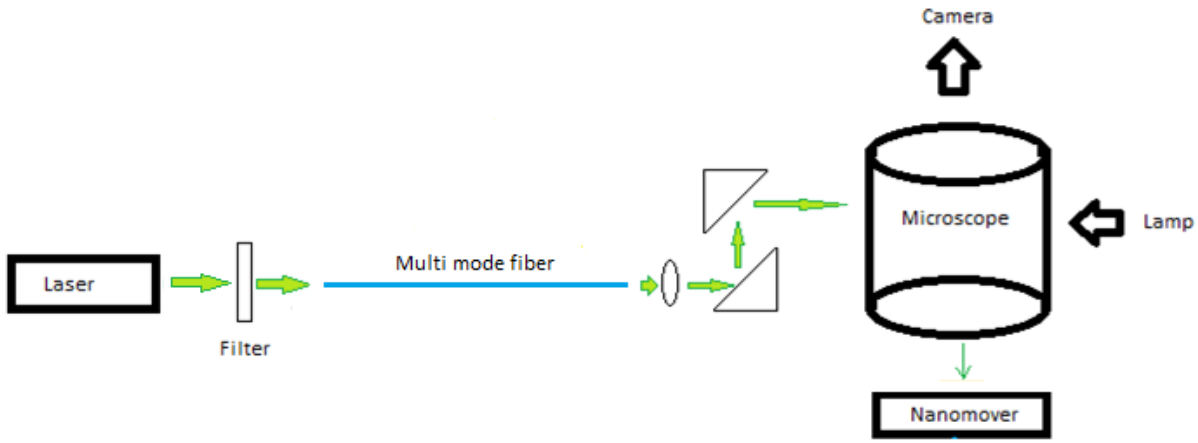

Figure 11: An illustration of the initial setup existing in the lab. This setup was to be developed for spatial photocurrent mapping.

4.2.1.2 Laser and laser fiber

For spatial resolution of the photocurrent it is important that the spot size of the beam hitting the target is minimized. The fiber connected to the laser was a multimode fiber which results in a large spot size. In a multi mode fiber the different modes will undergo random phase shifts and add up to an intensity that suffers from modal noise. For single mode fibers on the other hand there is only one mode and no modal noise. In the new setup a single mode fiber was to be applied. The fundamental mode of this fiber has similar spatial distribution to a Gaussian beam and may be focused to a diffraction limited spot which is not the case for the output from a multimode fiber [29].

Coupling light into the single mode fiber is challenging due to its small NA. At the aperture of the fiber there was a focusing lens which further enhanced the challenge. A small laser beam wouldn't be successfully focused onto the fiber core and result in large intensity losses. [30] Therefor a beam expander is used to increase the beam width to a collimated beam covering the lens aperture of the fiber. This results in a beam intensity of $1 - 1.6\ mW$ at the fiber output which corresponds to at least a third of the source intensity ($3\ mW$). Such a decrease could be expected as the beam is directed through mirrors, lenses and fiber and is a fully acceptable intensity for the purpose of these experiments.

4.2.1.3 Current measuring instrument

The current can either be measured with an ammeter or a Lock-in Amplifier (LiA). Two advantages of the LiA are that it measures only the signal with the same frequency as a reference signal which allows selective measurements of laser induced photocurrent and it gives a high signal-to-noise ratio.

The ammeter on the other hand could theoretically have faster measuring frequency than the LiA which would be advantegous in these measurements. The ammeter available however, showed to be slow in computer communication. Therefor the LiA was chosen and it was kept in mind that the measuring time should be kept as low as possible, important parameters are described bellow.

Lock-in amplifier

LiAs are used to detect small AC signals because of their ability to reduce noise (even a thousand times larger than the signal). They are so called phase sensitive and use a reference frequency to sort out signals with this specific frequency and phase. This way any noise with frequency different from the reference frequency will be filtered away allowing for measurements that are less sensitive to

surrounding environment. In this setup it would mean that the spatial photocurrent mapping could be carried out conveniently in a bright room which also improves laser safety.

The LiA first multiplies the signal with the reference signal (RS), which is a pure sine wave. An incoming signal may consist of a pure sine wave or multiple sine waves of differing amplitudes and phases. For a signal with multiple sine waves all components will be multiplied with the RS simultaneously. The average of a two sine wave product will differ from zero only if the frequency of the two waves is exactly the same. This is used to filter the signal in the LiA. This removes all components in the measured signal that has a different frequency than the reference signal and leaves the single Fourier sine component of a signal at the reference frequency.

A square wave signal (as in this setup) is, according to Fourier's theorem, represented by the sum of sine waves of different amplitudes, frequencies and phases. The LiA will filter out the first sine component from the signal. It measures over multiple periods and displays the RMS value of the signal. [31] The number of periods over which it measures is set by a time constant (TC) which should be minimized to achieve low measuring time. This requires a high reference frequency that allows the LiA to measure over several periods in shorter time. The RS frequency in this setup is generated by a light chopper placed in front of the laser beam which was set to a frequency of 3 kHz. For a TC of 10 ms the LiA measures over 30 periods. It is important that the induced current varies with the same frequency as the reference one. Parameters such as capacitances in the NWSC may limit the speed of its response to the alternating incident light.

The dynamic range is another parameter to take into account. One wants to be able to resolve small features in current change while also distinguishing larger steps in current, as when crossing the border of the device. This characteristic is governed by the sensitivity factor which should be set to appropriate value before every measurement. The measurements, shown in Figure 12 is an example of a successful scan with appropriate TC and sensitivity.

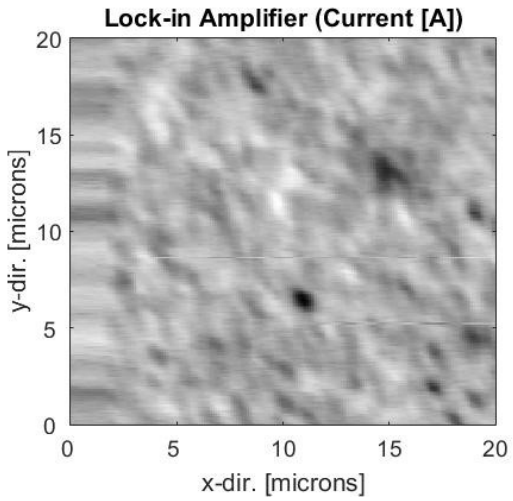

Figure 12: Scan using the LiA (100 nm/step) with appropriate settings of TC and sensitivity resulting in a high resolution scan.

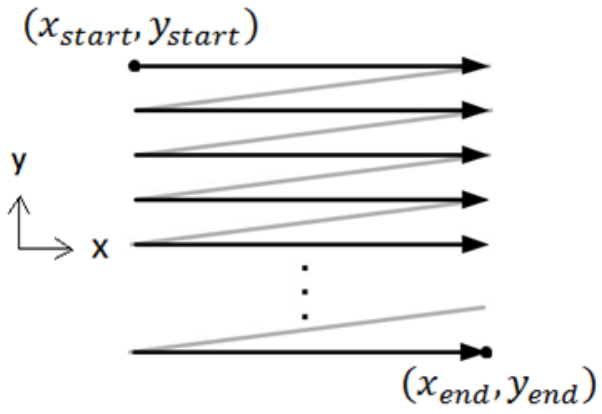

Figure 13: Illustration of scanning movement. Measurements are done along the horizontal, black lines (black) while the green lines show the translation movement between those lines. (Modified image [32])

4.2.1.4 Translation stage

A computer controlled translation stage that allows movement in two directions is used for performing the scanning movement in this setup. During an image scan the translation stage will

perform sweeps as illustrated in Figure 13. The speed is constant along every sweep in the x-direction. With a certain time span between measuring points the current is measured as the scanning movement is performed. For high resolution this requires that the LiA has a consistent measuring time and that the measurement is fast in relation to the speed of the scanning movement.

4.2.1.5 Computer communication

LabVIEW is the Software used to communicate with the translation stage and the LiA.

Several LabVIEW programs are used for different stages in the SPCM. The first important program is one that allows the user to move the translation stage for placement and investigation of the sample. The movement is steered using a joystick and the LabVIEW program allows the user to save important coordinates in the sample plane.

The second important program is the scanning program. This was already well implemented and initially only a few modifications were made to include the newly installed setup parts. This meant changing GPIB addresses and adjusting the computer communication for the relevant current measuring instrument.

4.2.1.6 Custom-made setup parts

Some hardware and setup parts were custom-made. A new joystick was made in order to facilitate movement with the translation stage for monitoring of the sample prior to scanning measurements.

In order to easily interchange between the SPCM setup and the angular dependence setup (explained in section 5.2), a custom-fit solution was made. Two metal plates were designed; one for permanent attachment to the sample and one for attachment to the two different setups used in this thesis. The second plate could be attached to both setup 1 and setup 2 by using different screw hole patterns.

4.2.1.7 Final focus optimization

To get familiar with the NWSC sample images covering the 1x1 mm^2 cells were taken. These images gave an overview of the cells indicating interesting areas for further investigation. Figure 14 shows such an image. The white area is the area covered with conducting ITO where the current is induced. The dark regions indicate areas with no or low current. The dark square surrounded by the white area corresponds to the gold contact where current is collected but not induced.

Comparing Figure 14 with another image of a 1x1 mm^2 cell (Figure 15) a difference in resolution is seen. This demonstrates the importance of focusing the microscope and laser before every measurement.

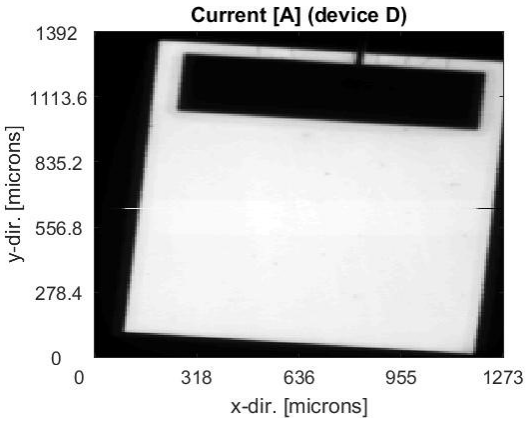

Figure 14: Device covering SPCM of device D.

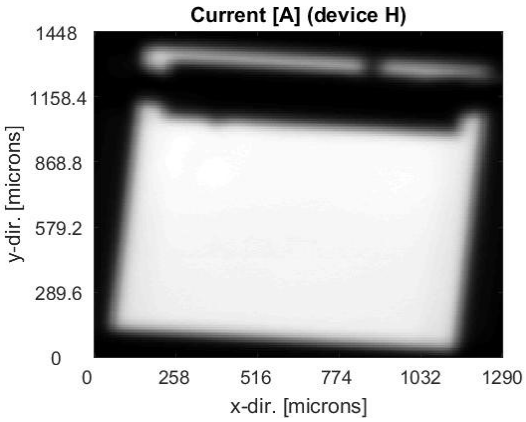

Figure 15: Device covering SPCM of device H. Example of a blurry scan due to poor focus and alignment.

The focus optimization came to include two things:

- An alignment and focusing procedure should be carried out before every image scan.
- An adjustable focusing lens at the end of the laser fiber was added.

The adjustable focusing lens allows the focus of the laser spot to be aligned with the focus of the microscope which would facilitate the focusing procedure.

For a scan across the entire 1x1 mm^2 device it is important that the device isn't tilted in comparison to the microscope objective. For the whole scan to be in focus the surface of the device has to lie within the focal depth of the microscope during the entire scan. This tilt was aligned by alternately changing the horizontal tilt of the device first in the x-direction and moving across the entire device along the same direction. This was done until the entire device was in focus along the line in the x-direction where after the same procedure followed for the y-direction.

Although the tilt has been adjusted to an extent that the entire device lies in focus the laser can be fine-tuned within the focal depth. To achieve this the laser was repeatedly scanned over a step while changing the focus. The photocurrent along the scan was plotted live in a graph together with its derivative. See Figure 16 for a picture of the plots from such a scan. The focus was this way set to its optimal point resulting in the smallest FWHM for the derivative of the photocurrent step. In Figure 17 it is clear that the red line has the lowest FWHM and thus that corresponding laser focus would be optimal (out of the three tested). The resolution will be further discussed in the results (section 4.4.2).

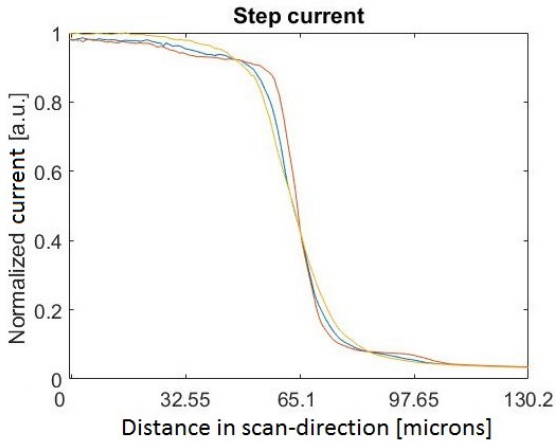

Figure 16: Current across a step (corresponding to crossing the border of the device) for different focusing of the laser.

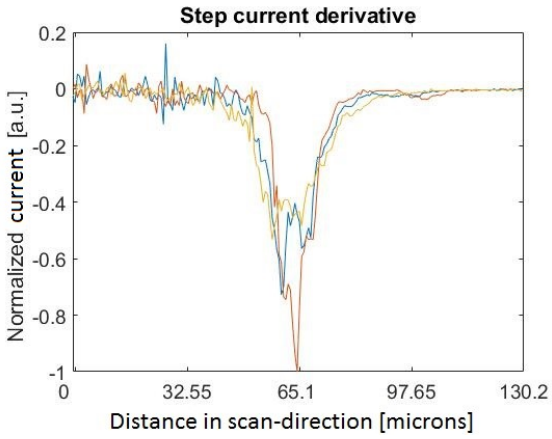

Figure 17: Derivative of the current shown in Figure 16.

4.2.1.8 Laser intensity measurement

To determine that the intensity fluctuations in photocurrent in the SPCM images were not results of intensity fluctuations in the laser itself, the laser intensity was investigated. This was done by measuring the intensity with a photodiode connected to the LiA. The LabVIEW measurement program was then set to sweep across an entire device to measure over a time span corresponding to such a sweep. The measured parameter was the intensity of the laser instead of the photocurrent of the sample. These measurements established that the laser intensity was stable over the time range that is relevant for the SPCM with low noise and no noticeable periodic fluctuations.

4.2.1.9 Reflection detection

Motivation

Measuring the reflection simultaneously as the photocurrent will give additional information in terms of characterizing the device and give a greater understanding of the spatially resolved absorption in the sample. In contrast to for example a microscopic image this will give simultaneous information about the reflection and complements the current in both time and space. In this sense the reflection detection is valuable.

Setup

To measure the reflection a photodiode was to be used. This was mounted at one of the microscope oculars and connected to a second LiA (LiA2) with the same reference frequency (the light chopper frequency). The LabVIEW program had to be modified in order to communicate with two Lock-in Amplifiers.

Ideally the current and reflection would be measured at exactly the same point in both time and space, which are closely related in this scanning procedure. The LiA2 was of an older model and possibly had slower computer communication. The initial plan was therefor to start the LiA2 and closely thereafter start LiA1. The LiA1 would be read out first followed by reading out LiA2, see illustration in Figure 18 a.). This would give LiA2 more time to respond while still diminishing the time between reflection and current measuring points.

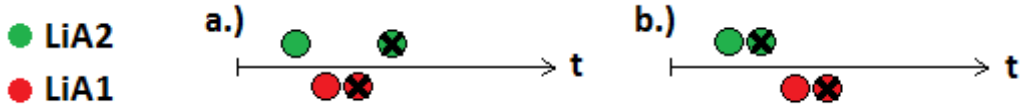

Figure 18: Illustration of time between measuring points and read out points for LiA1 and LiA2. Solid circles illustrate points where the current is measured while crossed points are illustrate the value being read out, sent to the computer. a.) scenario where the two LiAs are started right after one another, LiA1 is read out first followed by the LiA2 read out. This gives low time span between measuring points and long processing time for LiA2. b.) scenario where the LiAs measure and read out right away, first LiA2 and then LiA1. This gives slightly larger time span between measuring points.

Scans using strategy a.) in Figure 18 showed entirely dark rows in the reflection, rows where no data had been read out from LiA2, as seen in Figure 19. This scan is taken at the border of the gold contact in order to see how the detection performs for high reflection (laser beam incident on the gold contact) and low reflection (laser beam incident on absorbing nanowires).

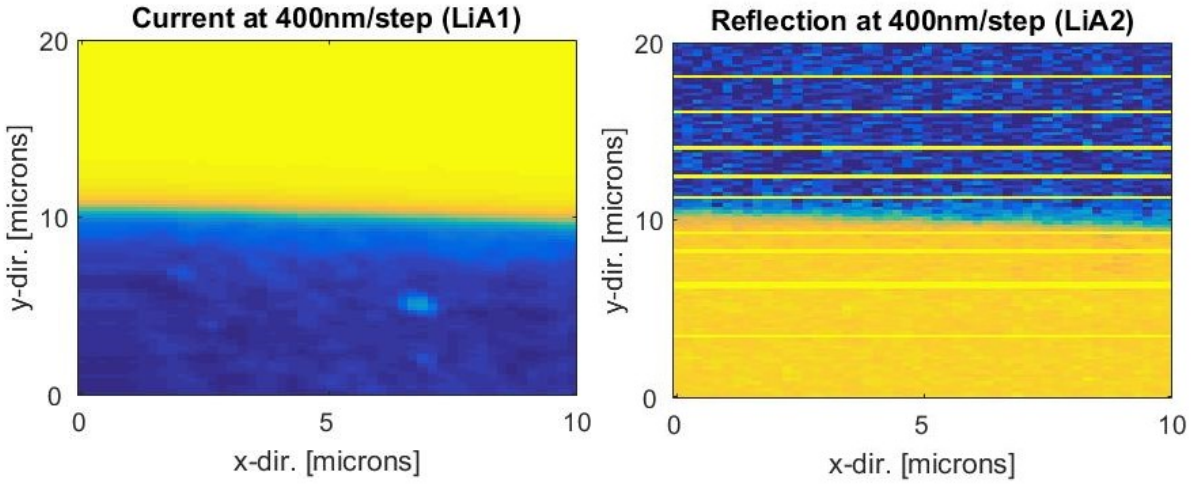

Figure 19: SPCM scan with simultaneous reflection detection over area covering the border of a gold contact toghe. LiA1 measures current while LiA2 measures reflection. The reflection scan shows dark rows which reveals that LiA2 fails to send data.

The read out sequence as in Figure 18 b.) was instead tested and surprisingly showed superior results to strategy a.). One LiA at a time was started and read out right away resulting in slightly longer time span between the measuring points but better LiA performance. Successful images were taken using this strategy and it was deduced that the slight shift in measuring points between current and reflection image was negligible.

4.3 Measurements

Photocurrent images (PCI) have been taken along the way with the development of the setup. Some images were used as indications of how to develop the measurement setup but may at the same time give information about the NWSC devices. The first images covering the 1x1 mm^2 cells (taken before the addition of reflection detection) are good PCIs for giving a first impression of the performance of the devices on the sample.

After the alignment procedure and final focusing optimization had been implemented PCIs with a resolution of 100-400 nm were taken. This was done at device borders and covering defects that

were visible in the optical microscope. These images are good results for investigating the resolution of the setup but also to look into features in the NWSCs at the 100-400 nm scale.

Once the reflection detection was in place both images covering entire cells and smaller high resolution images were taken, this time with additional information provided by the reflection image (RI). Images of entire cells investigate the correlation between the features observed in the PCI and those observed in the RI. This can simplify characterization of different defects. In section 4.4.3 discussions will be made within this topic.

4.4 Results and Discussion

In this section the results of the SPCM is presented and discussed. It must be said that the devices on this NWSC sample show very high quality with high currents and little defects. In that sense their design can be said to be successful. Further development and improvement is however always desirable. An attempt to identify defects, their effect on the performance and their origin is made in the following section, something that turns out to be rather difficult due to the high quality of the devices.

Table 1 shows characteristics provided by Sol Voltaics who characterized the sample after production (information about device H is missing and not presented by Sol Voltaics). In the analysis of the results the values given in Table 1 will be used as complementary information.

Device	V_{oc} [V]	I_{sc} [mA]	J_{sc} $[mA/cm^2]$	FF	Efficiency
J	0.537936	**0.211**	**20.100884**	53.73699	**5.810575**
F	0.542978	0.206	19.677738	53.77271	5.745392
D	0.537642	**0.211**	20.086674	52.54499	5.674566
B	**0.543142**	0.207	19.750202	47.71999	5.118998

Table 1: Device information provided by Sol Voltaics [33]. Measurements made at room temperature (298 K) for 1 sun illumination.

4.4.1 Images of entire 1x1 mm² cells

The first PCIs of the entire devices were used to get an impression of the NWSC devices. The PCIs showed high, even current across the devices with some surface artifacts that influenced the photocurrent. From the images an average current of the different devices was calculated, values presented in Table 2.

Device	Average Current [µA]	Comment
B	0.1215	Device has artifacts (fabrication remnants?) on top of surface
D	**0.1237**	Device surface looks smooth and blank, gives the highest current of all devices.
H	0.1137	Device covering picture was out of focus - may give unreliable value of the average current
J	0.1206	Device has some artifact on surface. Further investigation needed to determine if they are grooves or deposited on top.

Table 2: Average current per measuring point, for the different devices on the sample calculated from the first device covering PCIs.

D, which has a blank surface in the PCI, gives the highest current. The lowest average current is found for device H. This value is however not as reliable since the image was out of focus and may have influenced the detected photocurrent.

Comparing the values in Table 2 with the information given by Sol Voltaics (Table 1) shows some correspondence with D giving rise to the highest current. It is noticed however, that device J in our measurements has shown a lower current relative to the other devices. Sol Voltaics found that J and D had equally high short circuit current. It may be interesting to look into why J is showing reduced performance in the PCI. As J was showing some artifacts it is reasonable to think that these are affecting the performance.

The difference in measurement procedure behind these current values may affect the difference between them. Sol Voltaics measured using a broad light source with 1 sun (1000 W/m^2 = 1 mW/mm^2) intensity, whereas the SPCM was carried out with a highly focused laser beam of around 1-2 mW. This means a great difference in light intensity incident on single nanowires in the two cases. With an estimated spot size of 1 µm the laser light intensity will be in the order of 1 W/mm^2, at least three orders of magnitude higher than for 1 sun illumination. This is reason to believe that any tilt[1] or variation in thickness on the device may have a greater impact in the SPCM than in Sol Voltaics' measurements which may be the origin to the different relations between device J and D.

4.4.2 High resolution images

Images with higher resolution were taken in order to test the setup performance but also to look at device characteristics.

- Can the periodic pattern of nanowires be distinguished?
- Can single nanowires or single defected nanowires be resolved?
- What is the effective resolution of the setup?

Images covering the border of the device showed periodicity along the edge. Was this demonstrating the performance of individual nanowires standing in their periodic pattern? Figure 20 shows a border image and a 3D plot corresponding to the photocurrent values of the PCI. The resolution of the PCI is 100 nm/step and consists of 200x200 pixels. The periodicity along the edge seems to correspond to around 4.2 µm/period which is much more than the distance between neighbouring NWs. If the edge of the device does not have a border perfectly aligned with the NW pattern the periodicity along the border would not be the same as the size of the NW pitch as demonstrated in Figure 20. This border geometry would mean that a border periodicity of 4.2 µm corresponds to NWs at the edge for every 8^{th} pitch.

[1] For a 1 mm^2 NWSC sample a tilt of a tenth of a degree (a tiny tilt that could be missed during the tilt alignment) would mean a height difference between two sides of the sample at the scale of the diffraction limit. This means that the tilt could have an impact on the laser spot hitting the sample.

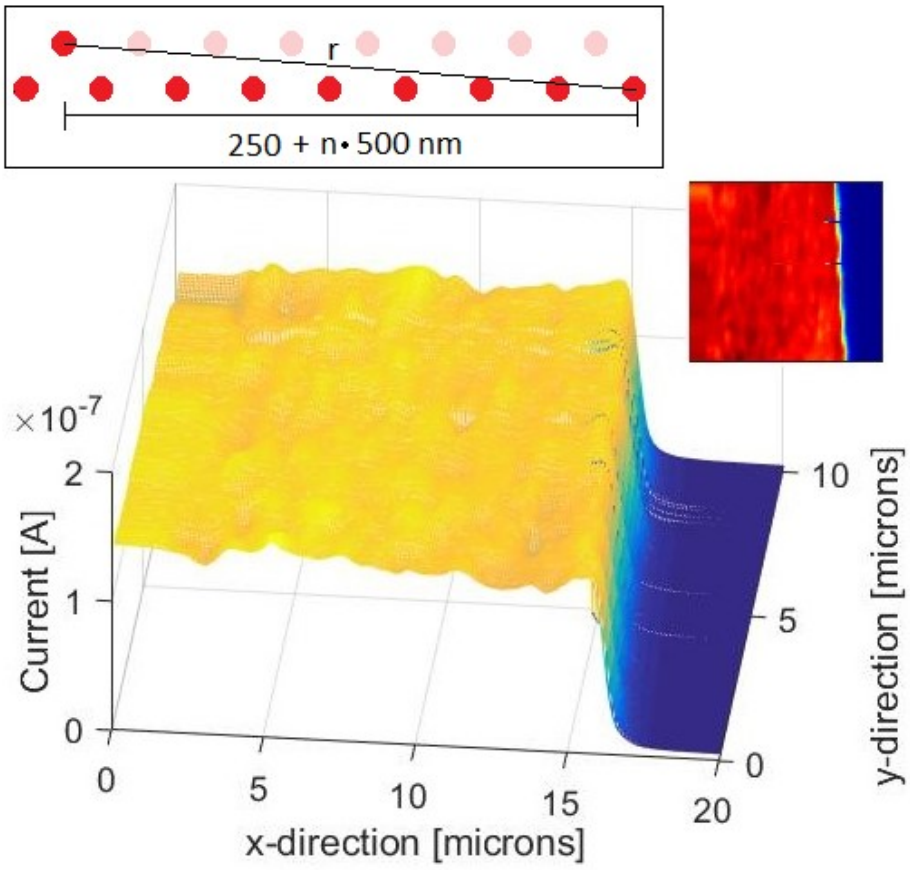

Figure 20: A scan of the border of device D with 100 nm/step shown as image and as 3D plot. At the top left corner is an illustration of the how the nanowires may be aligned at the border, the tilted black line would be the direction of the border r the periodicity showing up in the PCIs and in the number of NW pitches that gives rise to that periodicity.

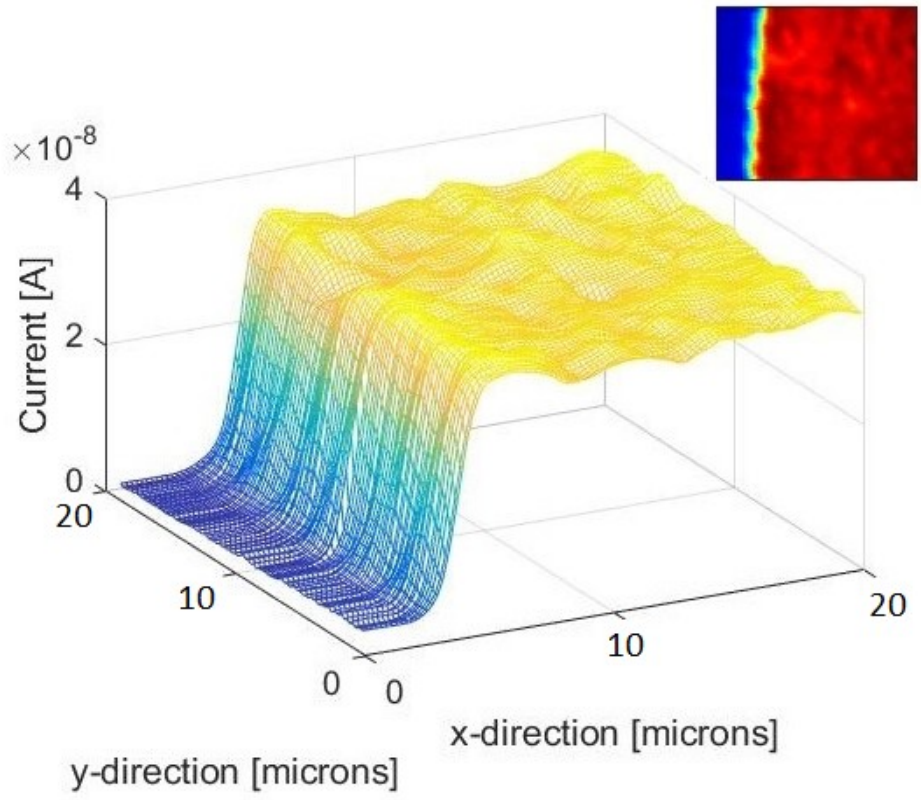

Figure 21: A scan of the border of device D with 200 nm/step shown as image and as 3D plot.

Figure 21 shows a periodicity of around 3.3 µm/period and according to the geometry shown in Figure 20 this corresponds to 6 NW pitches. The difference in periodicity between Figure 20 and Figure 21 would in such case be due to difference in alignment between border and NW pattern.

So yes, a periodic pattern is seen along the borders but it cannot be determined that the periodicity arises from single nanowires. Nor can it be excluded as the explanation given in Figure 20 supports the possibility. To further deduce this other characterization of the device, such as SEM, would be needed.

To further investigate if the photocurrent from individual nanowires can be resolved, high resolution images were taken at the center of the devices. Parts with visual defects are the most interesting to analyze. Such images were taken of device J and are shown in Figure 22.

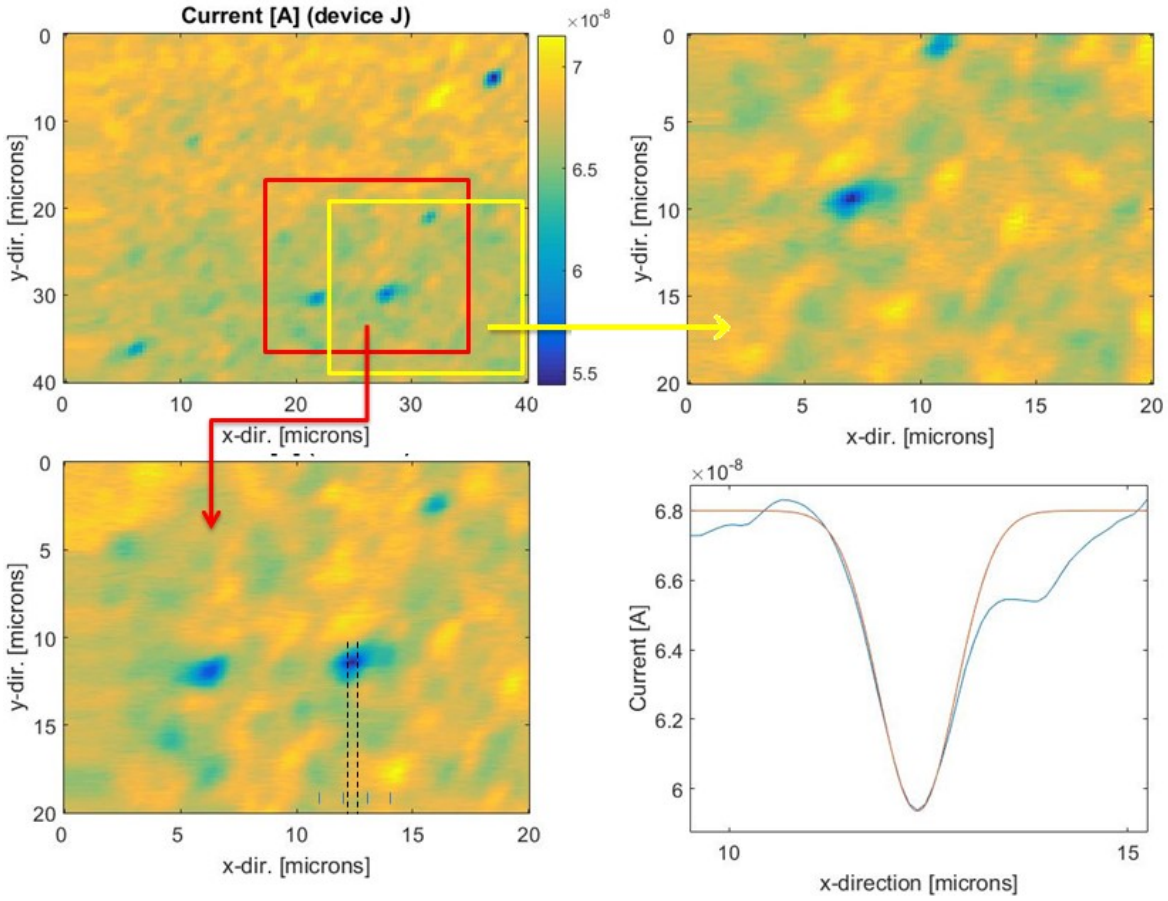

Figure 22: High resolution images with step size of 400nm (upper left), 200nm (upper right) and 100nm (lower left). Image taken of device J was over an area with dark spots. The lower right graph shows a current line extracted from the lower left image across the marked dark spot (blue line). A Gaussian beam has been fitted to the current line for identification of the 1/e2 point (red line).

In the first image (400 nm/step) we see dark spots on the scale that could correspond to single nanowires. When zooming in (100 nm/step) the center of the two darkest spots cover around 500 nm – the size of a NW pitch. It is highly possible that this is a spot corresponding to a single nanowire, either missing or defected giving rise to low current. The non-zero photocurrent may, as in [28], arise from the laser spot being larger than the resulting distance between two wires or by the large NW absorption cross section. Whether the nanowire is missing, badly contacted with ITO or has limited

internal quantum efficiency cannot be deduced from these images. The PCI would then need to be compared with information earned with other techniques. SEM could show the physical state of the NW while reflection and transmission detection combined with the PCI could be used for calculation of the spatial IQE.

Figure 22 shows the highest successful image resolution yet achieved with this SPCM setup. It will be used to estimate the resolution of the setup by identifying the size of the smallest resolvable feature. The dark dots previously mentioned show such features. The current is extracted from a line across the dark spot (marked in Figure 22) and a Gaussian function is fitted to the curve. Assuming that the laser beam intensity is described by a Gaussian function it is reasonable to presume that a dip in current will be imaged with a Gaussian profile.

The spot size of an ideal laser beam (described by a Gaussian function) is normally defined as the diameter between the two points where the intensity is $\frac{1}{e^2}$ of the total intensity. Half the value of the spot size can be said to give the resolution. By estimating the $\frac{1}{e^2}$ value for the curves in Figure 22 and taking half that value, the resolution is approximately 1 µm as compared to the theoretical value of around 405 nm.

Using a Gaussian diameter definition for the laser beam spot size in a laser scanning application can be considered constricted [26]. Another way of defining the spot size would be as the FWHM. Half the FWHM diameter value is around 0.55 µm which is another estimation of the resolution.

4.4.3 Simultaneous Reflection detection

Simultaneous reflection detection is one way of receiving complementary information to that given by the PCI. The reflection image (RI) will in principal give the inverse image of the PCI and any deviation from this presents new information about the device and its properties.

Three device covering images were made of device D, F and J shown in Figure 23, Figure 25 and Figure 28 respectively. These images were used to take a closer look at different types of artifacts.

4.4.3.1 Device D

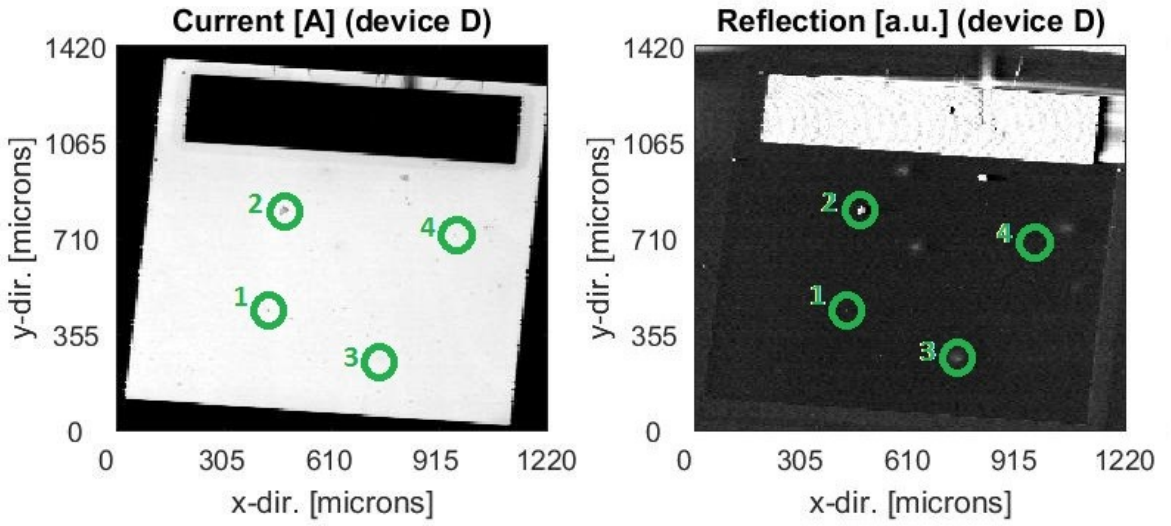

Figure 23: Device covering image of device D showing PCI (left) and corresponding RI (right), step size is around 6 µm. Different type of defects are marked and numbered in both images.

1. Defect 1 in Figure 23 shows a dark spot in the PCI and a bright spot in the RI. This could indicate a spot of missing nanowires. Since the reflection is slightly increased it indicates that the nanowire doesn't absorb the light. A possible reason is that the wire is missing and that the bottom substrate being flat increases the reflection. SEM or similar characterization would be needed to confirm this. In Figure 24 a.) the current has been normalized to the maximum current for the device and the defect shows to give around 65% of this value as compared to around 90% for non-defected areas close by. The defect is characterized by the sharp decrease in current accompanied by a sharp increase in reflection. Patches of missing NW should in principle give rise to zero current and the fact that this is not the case could again be due to the lasers spot size being larger than the NW pitch or due to the large cross-section of the nanowires meaning that surrounding wires absorb some laser light.
2. Defect 2 shows a larger artifact with high reflectance and low current output. This defect reduces the current to around 50% of the maximum value as is seen in Figure 24 b.). It is confirmed that the reflectivity is high. By investigation using the optical microscope it was confirmed that the defect was an artifact deposited on top of the device surface, could be metal remnants from manufacturing or different reflective material that has been attached to the surface during manufacturing.
3. Defect 3 shows a relatively large, diffuse bright spot in the RI in Figure 23. The photocurrent of the feature is not distinct, see Figure 24 c.). The defect increases the reflection but still gives rise to a relatively high photocurrent. This suggests that the NWs are intact and that the defect is located in the surface layer.
4. Defect 4 covers a spot that appears dark in the PCI but shows no particular increase in reflection in the RI, elucidated in Figure 24 d.). This indicates a defect in the nanowire itself, affecting the ability to generate or transport charge carriers. The zero increase in reflection could also be due to light being scattered away in all directions and not straight back to the reflection detector.

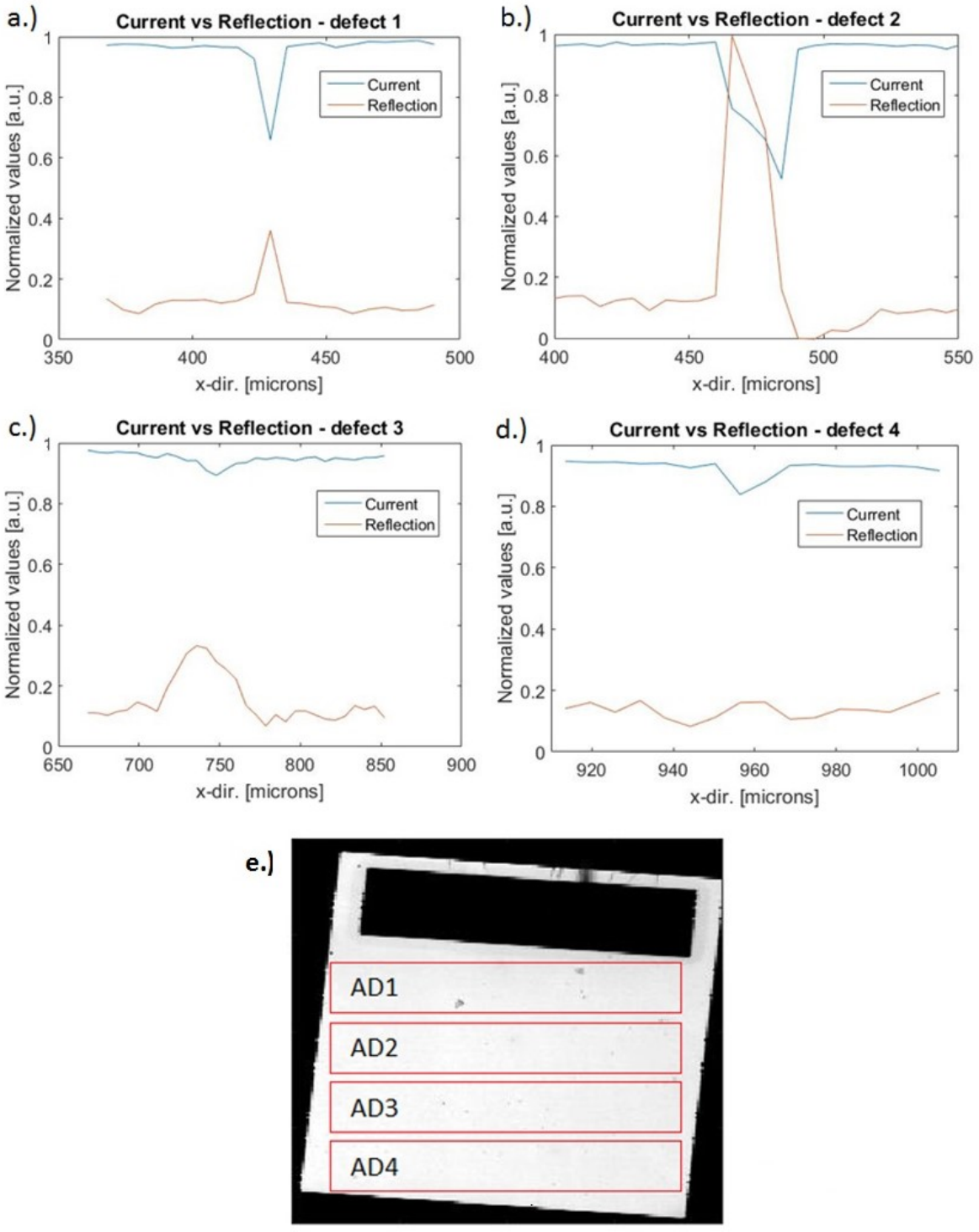

Figure 24: Lines extracted across different defects from the PCI and corresponding RI. This was done at a.) defect 1, b.) defect 2, c.) defect 3 and d.) defect 4. Figure e.) shows the device divided into different areas of the same size; AD1, AD2, AD3 and AD4 that will be used for current average calculations.

The PCI shown in Figure 23 was divided into 4 parts illustrated in Figure 24 e.) for calculations of average current presented in Table 3.

AD	Average current [µA]	Minimum current value [µA]	Comment
1	0.8566	0.4817	Area with lowest current (both average and minimum value). Also part with largest defects in PCI.
2	0.8789	0.6764	Area with high current, no (or low) visual defects in in PCI.
3	0.8795	0.6053	Area with high current, no (or low) visual defects in in PCI.
4	0.8800	0.7372	Area with highest current, no (or low) visual defects in in PCI.
-	0.8739	0.4817	Area with borders outlining the 4 sub-areas. Current value slightly lower than area 2, 3 and 4 but higher than area 1.

Table 3: Average current values per measuring point, calculated from the areas shown in Figure 24 e.) together with the minimum current value found in each area.

The results show that de performance of the device is affected by the defects observed in the photocurrent and reflection images. The total device average current showed a 0.7% lower value than the average in AD4. This is not a large difference but compared to a total efficiency of around 6% such a decrease does matter. It the entire device had as little defects at AD4 the efficiency could be improved.

The output current is well correlated to the amount of defects present in the area; AD1 showing the largest defects also has the lowest current while AD4 with least visual defects has the highest current. For this device the defected areas only seems to affect the current within that area.

4.4.3.2 Device F

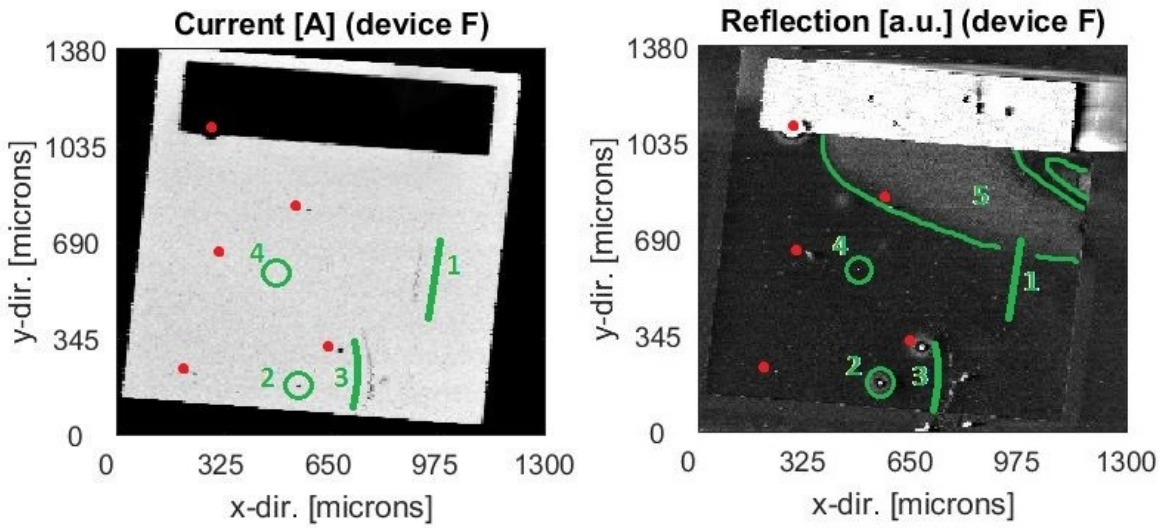

Figure 25: Device covering image of device F showing PCI (left) and corresponding RI (right), step size is around 6 µm. Different type of defects are marked and numbered in both images.

1. Defect 1 in Figure 25 shows a dark row in the PCI while not being visible in the RI. It is presumed to be a scratch of defected nanowires that still absorb light but don't give rise to any photocurrent.
2. Defect 2 shows a dark spot in current and a bright spot in reflection. Just as discussed for defect 1 on device D this could indicate a spot of missing nanowires. This defect follows the same current and reflection curves as demonstrated in Figure 24 b.). Similar defects are indicated by red dots.
3. Defect 3 is a bright line in the RI and a dark line in the PCI. It is more clearly visible in the PCI than in the RI which indicates a higher effect on photocurrent than reflection. This characteristic shows evidence of the same type of defect as defect 1. Defect 3 showed 10 times the current of defects 2.
4. Defect 4 covers one pixel and shows a low current in the PCI and high reflection in the RI. Same type of defect as defect 2.
5. The RI shows two artifacts that are not visible in the PCI, namely the two large brighter areas close to the gold contact and at the edge of the device (defect 5). Zooming in at the location bright reflection area in the PCI concludes that the artifact is not seen. The nanowires are working as they should but on the device surface imperfections slightly increase the reflection without notably affecting the photocurrent.

Figure 26: Shows the PCI in Figure 25 divided into different areas of the same size; AF1, AF2 and AF3 that will be used for current average calculations.

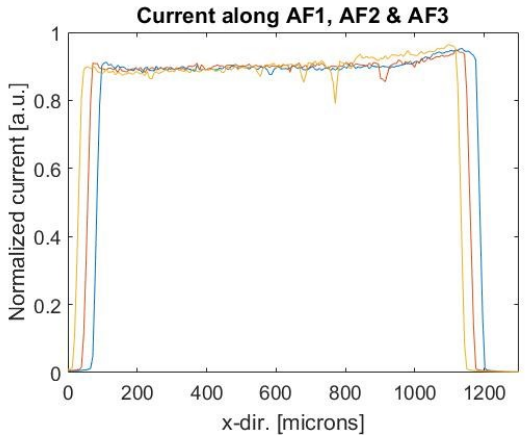

Figure 27: Illustration of current along the areas in Figure 26. AF1 – blue line, AF2 – red line and AF3 – yellow line.

AF	Device part investigated	Average current [µA]	Minimum current value [µA]	Comment
1	Covering roughly a third of device, close to gold contact	0.7091	0.1086	Area with lowest current but few visual defects in the PCI.
2	Covering roughly a third of the device, middle	0.7113	0.3783	Area with some visual defects.
3	Covering roughly a third of the device, upper part	0.7129	0.0308	Area with high current but the lowest minimum value. Area with most defects in PCI.
4	Entire device – area outlining the 3 subareas.	0.7115	0.0308	Current value slightly lower than area 2 and 3 but higher than area 1.

Table 4: Average current values per measuring point, calculated from the areas shown in Figure 26 together with the minimum current value found in each area.

From Table 1 where the current has been calculated for sections shown in Figure 26 it is obvious that the current is very stable over the entire device. The only significantly low minimum current value is found in AF3 which has the highest amount of visual defects in the PCI. The minimum current value is found at one of the dot defects. It is interesting however that AF3 is not the area with lowest average current, this is found in AF1 where there are very few visual defects in the PCI. This may be showing the effect of defect 5. This was investigated by looking at the current across the device in the horizontal direction for the different areas as shown in Figure 27. The result does not show decrease in current at defect 5. Instead it may be possible that high intensity or a slight tilt (as mentioned in section 4.4.1) has induced the difference in current between the areas.

4.4.3.3 Device J

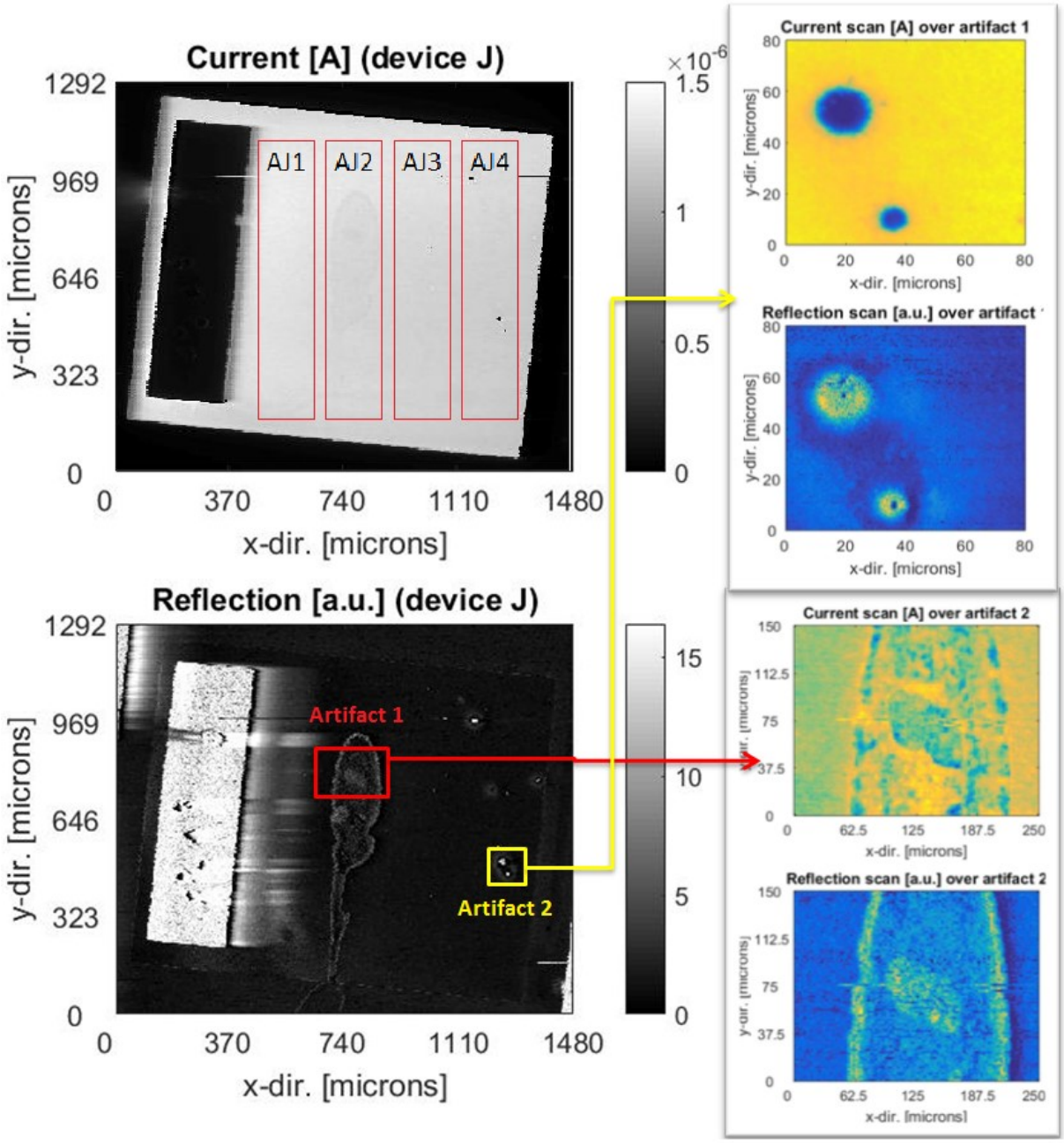

Figure 28: Device covering image of device J showing PCI (top) and corresponding RI (bottom), step size is around 3 µm. High resolution images, with step size 100 nm, of defects marked in the RI are shown to the right; red shows artifact 1 and yellow shows artifact 2.

A device covering image was also taken of device J together with high resolution images of artifacts on the device, see Figure 28. The average current was investigated over areas illustrated in Figure 28 and is presented in Table 5.

AJ	Average current, J [µA/pixel]	Minimum current value [µA]	Comment
1	1.339	1.252	Part with highest average current. Closest to the electrical contact and without defects seen in photocurrent image.
2	1.263	1.183	Area covering artifact 1.
3	1.233	0.629	Gives lower current than area 2, although covering no visual artifacts.
4	1.195	0	Are covering artifact 2 that gives rise to 0 current.
-	1.269	0	Area with borders outlining the 5 sub-areas. Current higher than area 2, 3 and 4 but lower than area 1.

Table 5: Average current values per measuring point, calculated from the areas shown in Figure 28 together with the minimum current value found in each area.

Judging from these results the type of artifact seen in AJ4 (artifact 2 in Figure 28) has a worse effect on the photocurrent than the type of artifact seen in AJ2 (artifact 1 in Figure 28).

AJ3 gives rise to lower average current than AJ2 despite the fact that AJ3 has no visual defects in the PCI. This indicates that artifact 1 may influence the ITOs' ability to conduct current. Any current induced to the right of artifact 1 would then contribute less to the total current than in the case of a perfectly conducting ITO.

To investigate the ITO performance lines for different y-values (direction defined in Figure 28) were extracted to compare the current for lines crossing artifact 1 with lines above and below the artifact. Figure 29 shows the result. There seems to be an overall lower current for lines at lower y-values. This is also intuitively seen in Figure 28, a feature that is not necessarily related to artifact 1. What is more interesting is comparing the blue and the red line. The red line crosses the defect at its widest part and shows a dip in current corresponding to this width. The current for x-values after the defect remains low which agrees with the assumption that artifact 1 affects the conductivity of the ITO.

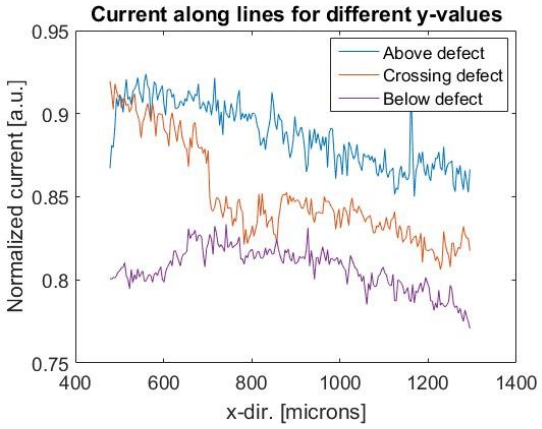

Figure 29: Current along the x-direction for y = 1180 µm (blue), y = 850 µm (red) and 180 µm (purple) in the PCI in Figure 25.

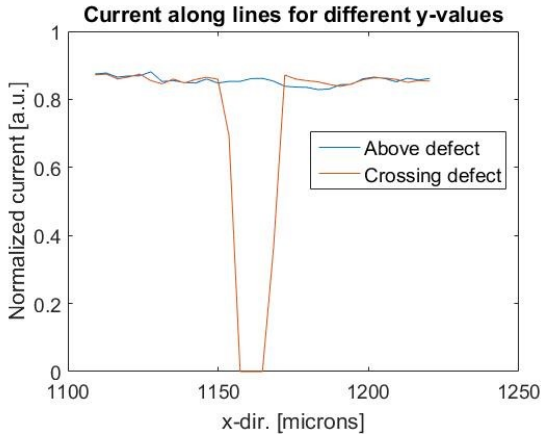

Figure 30: Current along the x-direction across the dot defect in the PCI in Figure 25 compared to a current line above the defect (with normal current performance).

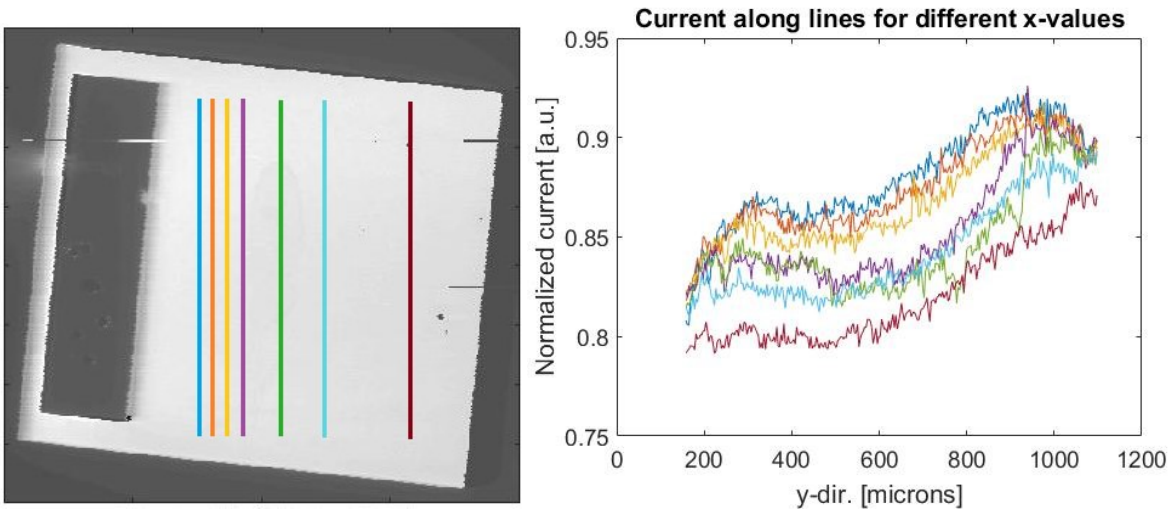

Figure 31: To the right: Current along y-direction for different x-values as illustrated in the figure to the left. Values are normalized to the maximum current value of the image.

Current lines extracted for different x-values in the PCI are shown in Figure 31. This is another way of investigating the influence of artifact 1. The current along the artifact is significantly lower than for lines to the right of it but the decrease in current with increasing x-value seems to start already before the artifact. This does not confirm the effect of artifact 1 on the ITO, rather the opposite. The gradual decrease indicates a different origin. The old device covering PCI of device J was then investigated in the same manner which showed a different current distribution. Here the current increased at the center and further away from the gold contact in contrast to the distribution seen in Figure 31 where it seems high along one side of the device. The old PCI was taken before the tilt-alignment-procedure was implemented and the high intensity condition may have a had a large influence. The comparison with the old device left further doubt to that artifact 1 influences the entire device by decreasing the ITO conductivity; it cannot be concluded nor completely rejected.

To investigate artifact 2 and to compare its influence on the photocurrent to that of artifact 1 a line plot was made, Figure 30. This makes it clear that artifacts of the type seen in artifact 2 have a grave effect on the generation of photocurrent as opposed to artifacts of type artifact 1 which induce only a low decrease.

4.4.4 Evaluation of scanning technique

The SPCM developed in this thesis showed to give successful measurements of spatially mapped photocurrent and corresponding reflection. The technique gave high resolution images but still demonstrates room for further development.

- Start blur, indicated in Figure 32 arises as result of the initiation time of the LiA. It could be accounted for by editing the scanning program and adding a dwell time at the start of every new line before measurements start to be recorded. The start blur is also a relatively small error and does not show for larger scans, in the work of this thesis it has been acceptable.
- Reflection saturation in LiA2 showed up in the RI as bright stripes along the scan direction as the scan passed a highly reflective area. When the sensitivity factor was increased the artifact diminished but the resolution got too low to resolve low-contrast-features such as borders of the device. Some reflection saturation errors thus had to be accepted in the RIs of this project. A way of reducing the saturation artifact could be to decrease the time constant

for the LiA. Another modification of the setup is to detect only a central spot of reflection, the directional reflection, which could be a way of increasing the accuracy.

- A further development of the setup could be to add quantitative measurements of the reflection together with transmission detection. This would enable calculations of spatially resolved IQE which is another interesting parameter of the NWSC.

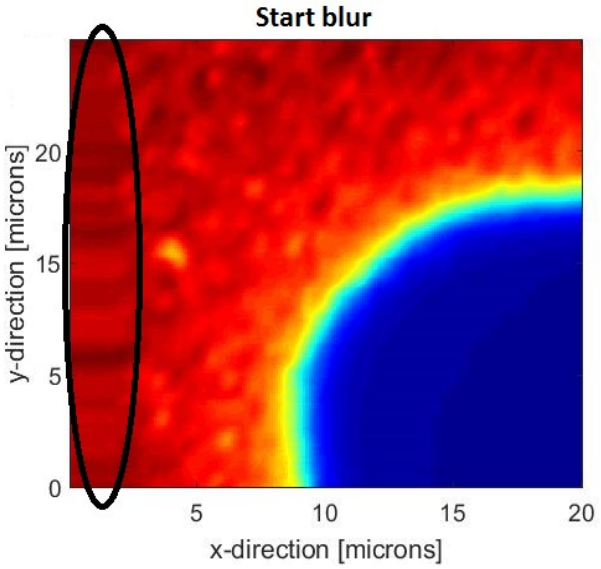

Figure 32: Image illustrating start blur. The step size is 100 nm.

5. Angular dependence

This chapter covers the investigation of angular dependence of the photocurrent. Theory behind the angular dependence is presented, the experimental setup explained, and the results are shown and discussed in comparison to the theory.

5.1. Theory

An expected angle-current dependence is the one resulting from the intensity decrease as function of angle. This dependence follows Lambert's cosine law and can for this case be described geometrically as follows.

The intensity is given by $I = \frac{P}{A}$ where P is the power of the beam and A its the area. The light source shows a relatively circular beam where the radius in the z-direction, will be unchanged as the incidence angle increases. The change in intensity will be governed by the change in beam area which in turn changes with radius in the y-direction (see Figure 33). This change in radius depends on the angle, θ, by $r_y = \frac{r_{y0}}{\cos\theta}$ where r_{y0} and r_y are the radius in the y-direction for normal incidence and for angles larger than normal incidence respectively. With r_z as the radius in the z-direction the intensity is then given by:

$$I = \frac{P}{\pi r_z r_y} = \frac{P}{\pi r_z \frac{r_{y0}}{\cos\theta}} = \frac{P\cos\theta}{\pi r_z r_{y0}}$$

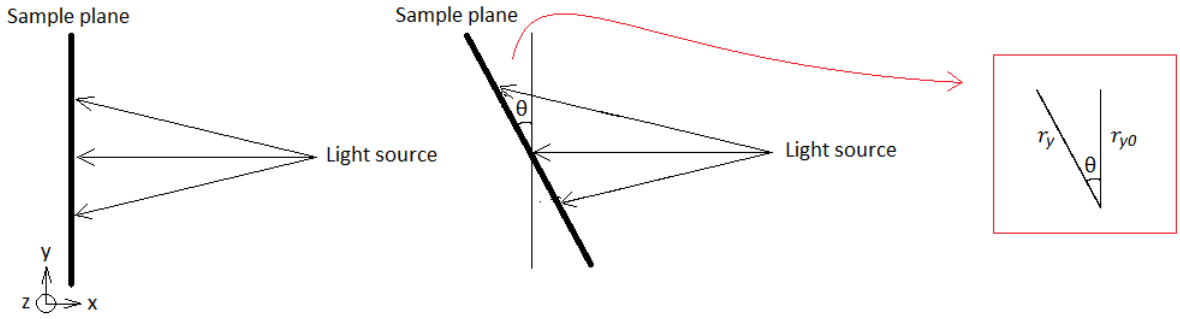

Figure 33: Illustration of light incident on sample and the change in spot size (on the sample surface) as the incidence angle changes. Sample at normal incidence (left), sample at angle θ from normal incidence (middle) and illustration of change in light spot radius at the surface of the sample (right).

For planar solar cells the short circuit current is proportional to cosine of the angle according to Lambert's law and illustration above. The dependence is however also influenced by other parameters [34];

1. The reflection depends strongly on the angle (further discussed in section 6.1) and also on the smoothness of the surface. This consequently influences the current-angular dependence.
2. At high illumination intensities the effect of internal series resistance might have an influence on the photocurrent. This is relevant for the angular dependence as the intensity changes according to Lamberts law.
3. The light that penetrates the cell surface will propagate with varying angles which may influence the absorptance and spectral sensitivity of the solar cell.
4. Lastly differences in reflection of linear polarized light (parallel vs perpendicular) may influence the current output.

The latter will be further discussed in section 6. Figure 34 shows the short circuit current for a silicon n-p planar solar cell as function of angle. The photocurrent is expressed as the fraction of current at normal incidence. In this figure the phenomena (1) can be seen as the curves (representing different illumination densities) all lie under the reference $cos\theta$ curve for higher angles. The study concluded that this was the case for incidence angles greater than 30° where the photocurrent was significantly smaller than expected from the cosine law and that it was mainly due to the reflection increase.

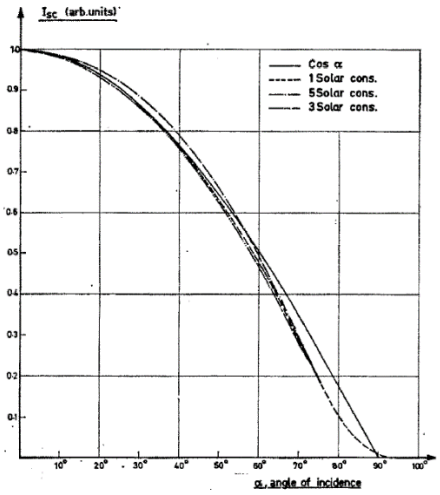

Figure 34: Short circuit current for a planar n-p silicon cell as function of incidence angle of light source. Current is normalized to value at normal incidence. Striped lines correspond to different illumination densities and the solid line is a reference line of cosθ. (Original figure [34]).

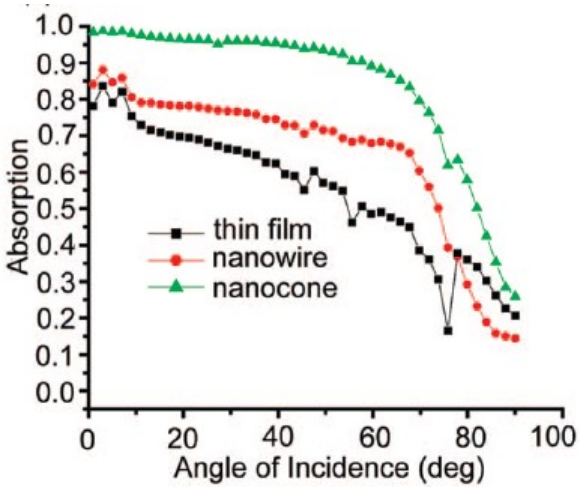

Figure 35: Absorption (at wavelength λ = 488nm) as function of incidence angle for different solar cell structures of hydrogenated amorphous silicon; Nanocone array (green) , nanowire array (red) and thin film (black). (Modified figure [35])

Figure 35 shows the measured absorption (at 488nm) of hydrogenated amorphous silicon thin film, NW arrays and nanocone arrays [35]. The nanowires were of 300 nm in diameter and 600 nm long. In this study the absorption decreased as the angle of incidence increased for all samples. According to the authors this was due to the reflection increasing with the incidence angle not only for the planar sample but also for the nanostructured ones. The highest absorption was seen in the sample with nanocones but it was also deduced that the sample with nanowires had a stronger absorption than the planar sample. The nanowire sample has around 65% absorption at 70° where the planar shows around 40%. For low incidence angles an increase in absorption is seen for the thin film and the nanowire array. At normal incidence, the authors explain, some of the reflected light escapes out from the port where the light source enters and result in the fluctuations of absorption at low incidence angles.

A study simulated the effect on reflectance of silicon nitride subwavelength structures for silicon solar cells [36]. The reflectance was, amongst other structures, investigated for cylinder shaped structures which corresponds well to the NW structure. The study was made using three dimensional finite element simulations. The cylinder shaped subwavelength structure had a diameter of 130 nm, height of 600 nm and a unit cell (pitch) of 200 nm and its spectral reflectance for different incidence angles (given in simulation) is shown in Figure 36. This result may be interesting for comparison with data results in this thesis. Doing this however, it should be said that the differences between the parameters used in the simulation and the parameters for the sample in thesis may give deviations in resulting reflection/absorption both in the specular and angular dependence. One such parameter is

the refractive index which is 2.07-2.00 for silicon nitride at 500nm to 800nm, compared to 4.41-3.46 for InP [37] [38].

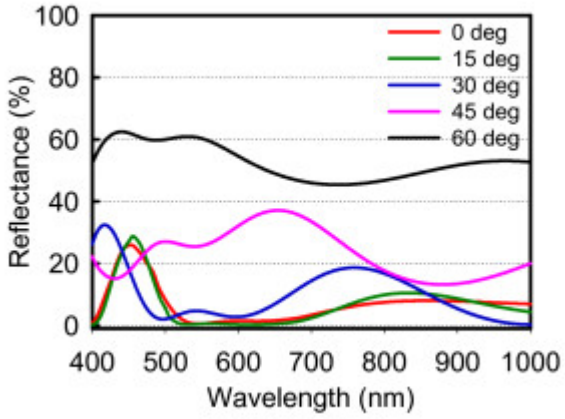

Figure 36: Spectral reflectance for cylinder shaped silicon nitride subwavelength structures on a silicon solar cell. Different lines show the reflectance for different angles of incidence. (Original figure [36])

5.2. Measurement setup

In the final setup as illustrated in Figure 37, a white broad band lamp is used as light source which is modulated by a Fourier Transform Spectrometer. The sample was mounted on a sample holder with two small translation stages in the y- and z-directions, Figure 38. The sample holder was attached to a rotational plate that allowed the light incidence angle to be changed.

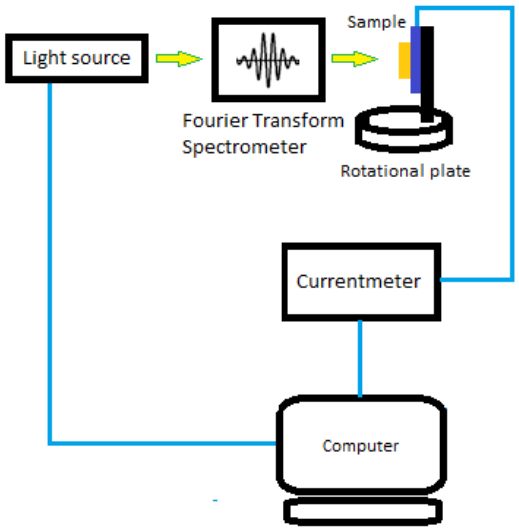

Figure 37: Final measurement setup for measurement of angular photocurrent dependence.

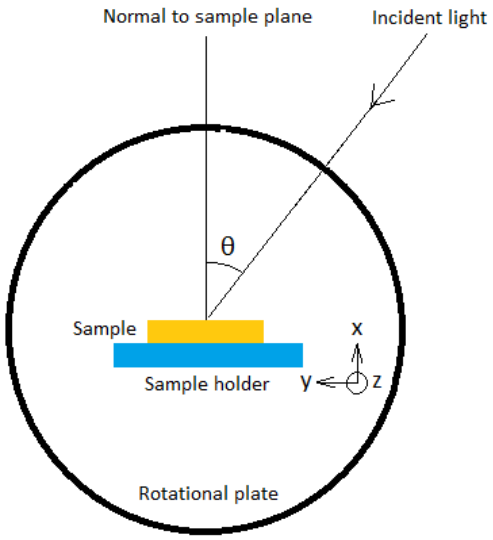

Figure 38: Illustration of sample placement in relation to rotational plate. Incidence angle, θ, and x-, y- and z-directions are demonstrated.

5.2.1. Light source

For this investigation it would be preferred to have a light source with a wide beam since this would mean a smoother intensity distribution and the beam would well cover an entire device. As the current-angle dependence might differ for incoming light of different wavelengths it would be

convenient to have a light source with tunable wavelength. First a supercontinuum light source was considered and the spectral intensity of the device was investigated. This showed a high intensity in the IR range but a rapid decrease reaching wavelengths of 450 nm and lower. For the NW array investigation wavelengths between 300nm and 900nm are of interest since this is their range of operation (roughly the range with EQE > 0) [21]. Consequently a new light source had to be found. Here a Fourier spectrometer equipped with three different light sources (white light source, UV and IR) was a possible solution. The white light source (in the visible range) and the UV light source were promising. Their spectra were recorded and the UV light source showed an irregular intensity distribution. The white light source however, showed good intensity for energies 1.3 eV (~950nm)-2.5 eV (~495nm) (Figure 39). The decrease at 1.3 eV arises from the band gap of the detector which in this case was a Si photo-diode while the decrease at higher energies corresponds to reduced light source intensity.

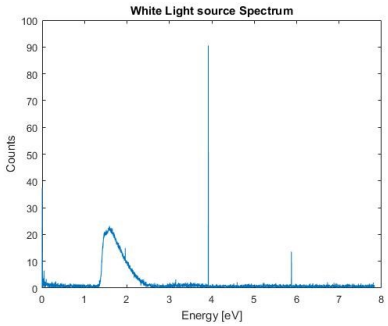

Figure 39: The spectral intensity of and the white light source of the Fourier transform spectrometer. Decrease at low energies originates from band gap of the detector material while the decrease for higher energies arises from the light source itself.

5.2.2. Fourier Transform Spectroscopy

This technique, in its simplest form, uses a beam splitter that directs part of the beam to a static mirror and part of it to a translation mirror placed as shown in Figure 40 [39]. During the measurement the translation mirror will be scanned over a known distance and an interference pattern between the two beams will be created containing spectral information of the beam. The signal is the Fourier transform of the light source spectrum, hence by Fourier transforming the given signal the spectral information is found. This technique has a great advantage since it uses the entire spectrum of the light source and the entire spectrum can be obtained simultaneously.

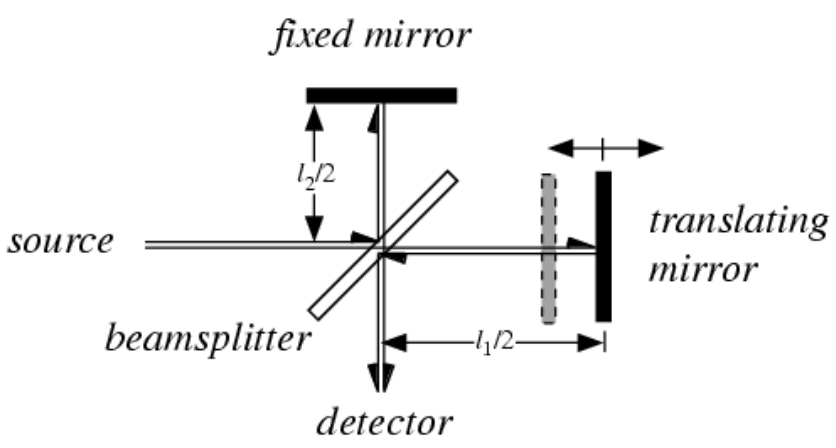

Figure 40: Illustration of a Fourier spectrometer. (original image [39])

5.2.3. Assembly of setup parts

This setup was assembled to meet the right measurement conditions. It had to enable positioning of the device at the right position in x-, y- and z- direction related to the light source (Figure 38 for illustration). It was crucial that the sample surface was placed at the center of the rotational axis in order to not introduce translational movements as the sample is rotated. It was also important that the 1x1 mm^2 devices were well covered by the beam and that they could be placed in the center of it. The setup was realized using different setup parts that were available in the lab and completed by making two custom-fit that tied the assembly together.

5.3. Measurements

The device to be examined would be placed at the center of the light spot at normal incidence. The current was measured at normal incidence followed by measurements for every 10:th degree of rotation in the xy-plane.

This was done for all the devices and twice for some of them. As the data was processed and investigated it was noticed that there was a large difference in the current output at low angles for the devices measured twice. It was then discussed that this could be due to variations in starting position between the two measurements. In order to make sure that the starting point was accurate (at normal incidence) the reflection of the light spot from the device was to be used for calibration. By rotating the sample so that the reflection exactly hits the incoming light spot the position would be accurately placed at normal incidence. The measurements were remade using this technique to increase consistency.

5.4. Results and Discussion

These measurements show interesting features and indicate a different angular dependence for the NWSC than for planar devices. The accuracy of these measurements is limited by the human factor. The starting position of the sample, at the center of the rotational plate and perpendicularly to the light source, was manually fixed. The rotation for every tenth angle was also manually changed. These things may influence the accuracy of the results. Multiple measurements would be needed for the results to be completely reliable. Nevertheless, they do show consistency and can be used as indications of the angular dependence and of features that are relevant for further investigations.

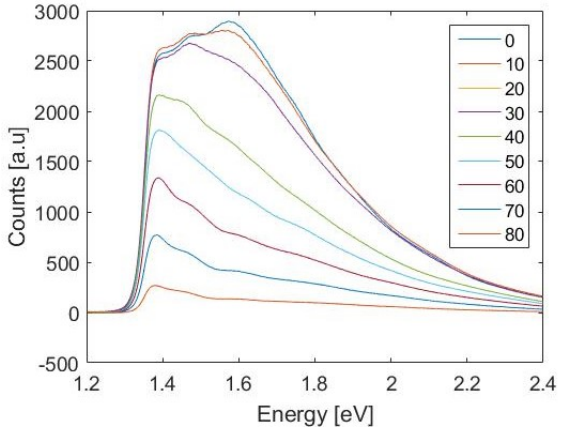

Figure 41: Intensity spectra for lines corresponding to different incidence angles. Results for device D.

Figure 41 shows the spectra for all measured incidence angles. Here the decrease in photocurrent is seen for energies around 1.3 eV which corresponds to the bandgap of InP and the intensity drops for higher energies as the power of the light source diminishes. It is also seen that the entire intensity curve is lower for higher incidence angles, something that can be mainly attributed to Lamberts law.

For comparison with Figure 34 in the theory the total intensity for every angle was investigated. The spectrum was integrated for energies between 1.3 and 2.2eV where the light source intensity was >> 0, result shown in Figure 42. Comparing the angular dependence to the reference cosine curve displays a similar angular dependence as the planar device (Figure 34 also shown in Figure 42 for easier comparison).

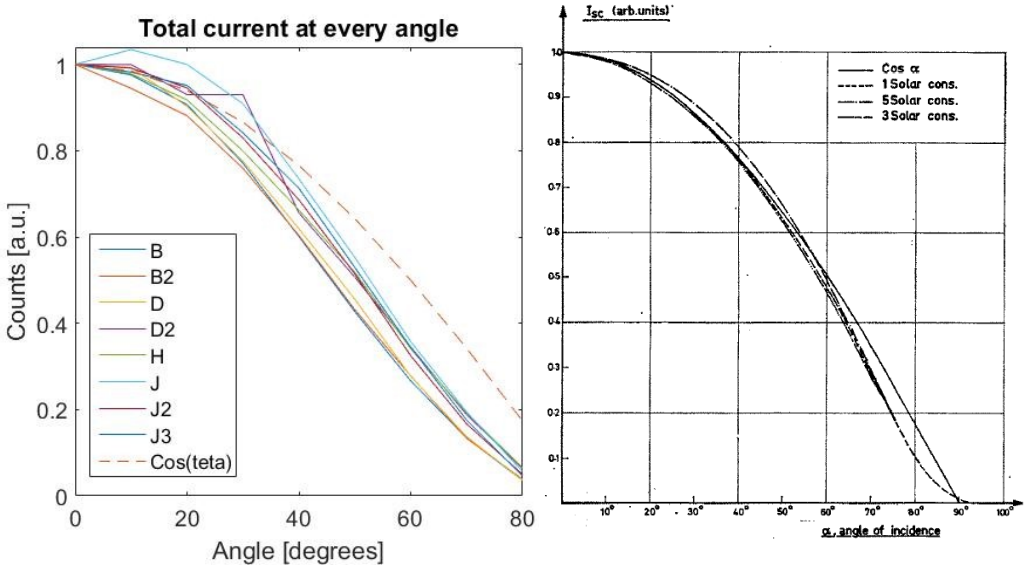

Figure 42: The total current intensity at function of angle for the different devices (left) and the current as function of angle for planar solar cell (Figure 34 shown here to facilitate comparison).

One measurement of device J is the only curve slightly deviating from the remainder. This measurement was made before the calibration of the starting position while measurements 2 and 3 of device J were made after and show consistency. The D2 curve shows a spike for 30° which is most likely a measurement error and can be neglected in this discussion.

For a thorough investigation of the NWSC dependence on incidence angle it is interesting to look at the performance at different energies. In Figure 43 the intensity as function of angle, normalized to normal incidence is shown for incident light of 900 nm, 700 nm and 500 nm respectively.

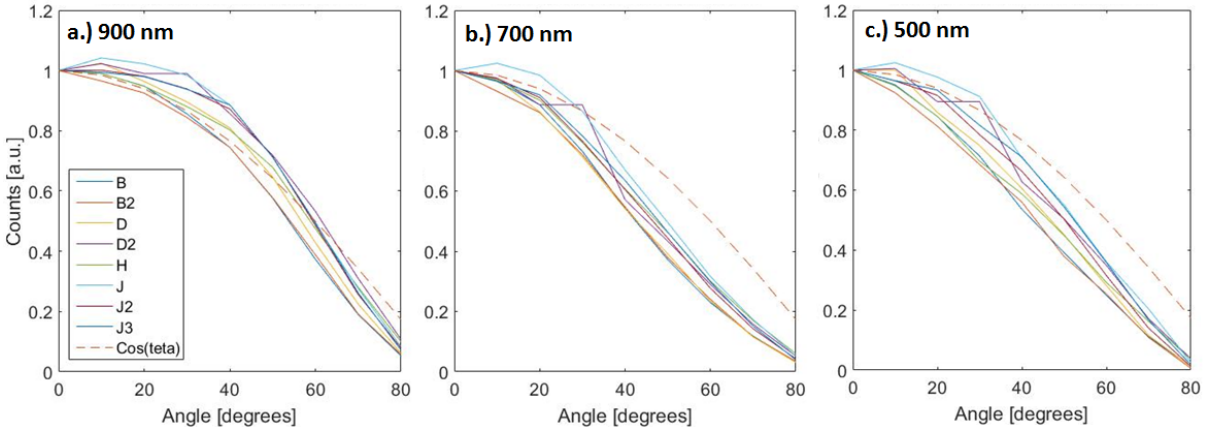

Figure 43: Current intensity as function of angle, normalized to the value at normal incidence for a.) 900 nm, b.) 700 nm and c.) 500 nm.

For 900 nm most device curves lie above the cosine curve for angles up to around 50-60 degrees and then go just slightly below the curve. The fact that the curves are above the cosine shows a better absorption and photocurrent generation than a planar device. This demonstrates the difference between a NW covered surface and a planar one as presented in Figure 35 in the theory. The theory demonstrated a case for different wavelength and geometry but still shows a behavior that is characteristic for a nanostructured surface as compared to a planar one.

The 700 nm curve shows an intensity below the cosine function for all angles above around 10° with largest difference for angles around 60°. This current decrease can be attributed to increased reflection as mentioned in the theory [34]. The intensity at 500 nm shows similar effects but with a more constant difference between measured results and cosine function. To further look into the difference in angular dependence at different energies Figure 44 were plotted, showing intensity curves normalized to the cosine law.

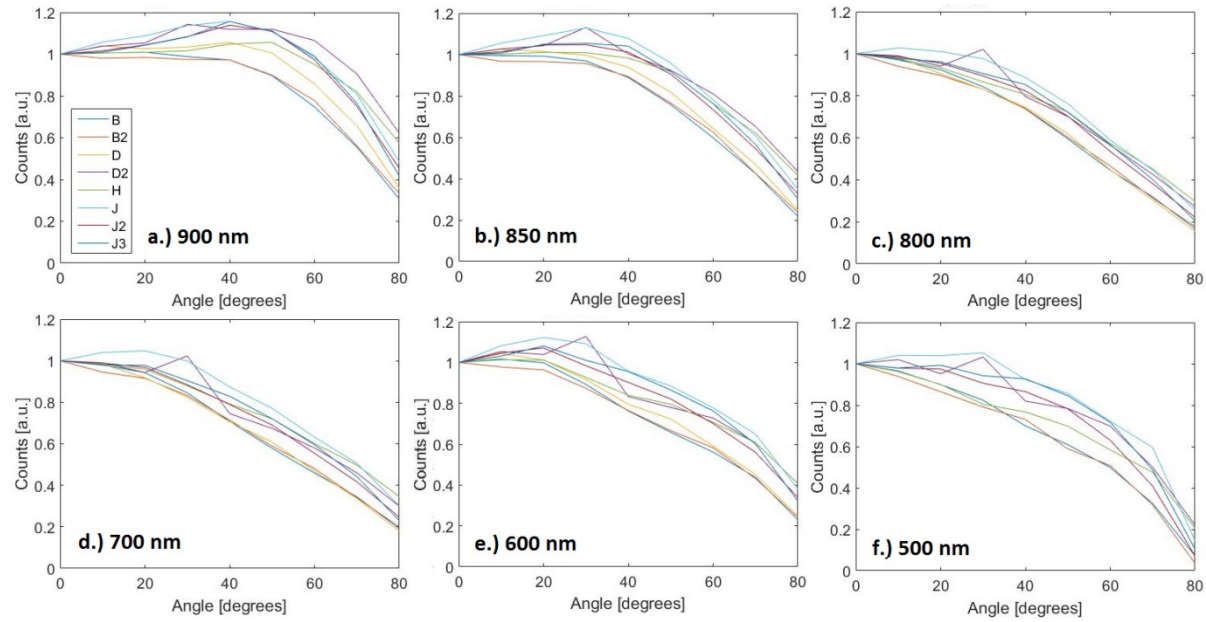

Figure 44: Current as function of angle normalized to the value at normal incidence and to the cosine law at a.) 900 nm, b.) 850 nm, c.) 800 nm, d.) 700 nm, e.) 600 nm and f.) 500 nm.

Figure 44 again confirms that the intensity for 900 nm follows the cosine dependence up until 50-60 degrees. For energies of 800 nm to 700 nm the intensity decreases quite linearly with increasing

angle which could imply a linear increase in reflection. Figure 36 in the theory supports this by showing a gradual reflection increase for energies around 700 nm. For 900 nm the same figure shows that the reflection doesn't increase significantly until 60° and for higher energies (up to 500 nm) reflection starts increasing significantly for angles above 30°. The former fits the measured results at 900 nm very well while the latter behavior isn't obvious but shows similar tendencies at 500 nm.

The angular reflection dependence for planar devices does not change significantly with energy, this behavior is characteristic for NWSC devices where light interaction with the nanowire structure affects reflection and absorption differently at different energies. The angular dependence will be affected by the NWSC geometry and the results shown in this thesis might not apply to other devices.

6. Polarization influence on angular dependence

This chapter presents theory and simulation of the solar cell polarization dependence at different angles and energies and shows experimental results of such measurements.

6.1. Theory

For planar devices the polarization dependence as light is reflected from a surface at different incidence angles is known [40]. This is described by the Fresnel reflection and depends on the refractive indices of the two media. Light with electric field parallel to the plane of incidence (P) will at some angle between 0° and 90° have a reflection coefficient of (or close to) zero, i.e. it will have a reflection minima. This angle is called the Brewster angle. Light with electric field perpendicular to the plane of incidence (S) will have a greater reflection [41]. Equation 1 and Equation 2 give the reflection for S and P polarized light respectively. Figure 45 illustrates the reflection between two media, the different light polarization directions and incidence and transmission angles, θ_1 and θ_2.

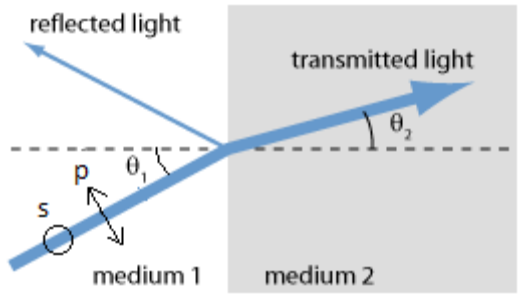

Figure 45: Illustration of reflection and transmission of light between two media. The incidence angle, θ_1 and transmission angle, θ_2 are indicated as well as the direction of different light polarizations (s and p) in respect to the incident radiation. (Modified figure [42]).

Equation 1

$$r_s = \frac{n_1 \cos\theta_1 - n_2 cos\theta_2}{n_1 \cos\theta_1 + n_2 cos\theta_2}$$

Equation 2

$$r_p = \frac{n_2 \cos\theta_1 - n_1 cos\theta_2}{n_1 \cos\theta_2 + n_2 cos\theta_1}$$

[41]

As mentioned in section 5.2.1 the refractive index for InP for light with wavelengths varying between 400 nm and 800 nm varies from 4.4149 to 3.4617. As result the Brewster angle also changes between 78.092° and 73.915° for the same wavelengths interval. The spectrum for S, P and nonpolarized light at an incidence light of 800 nm is given in Figure 46. For incident light of different wavelengths the curves will change slightly in accordance with the change in Brewster angle but the graph can be used as an indication of the polarization dependence for InP with a planar surface.

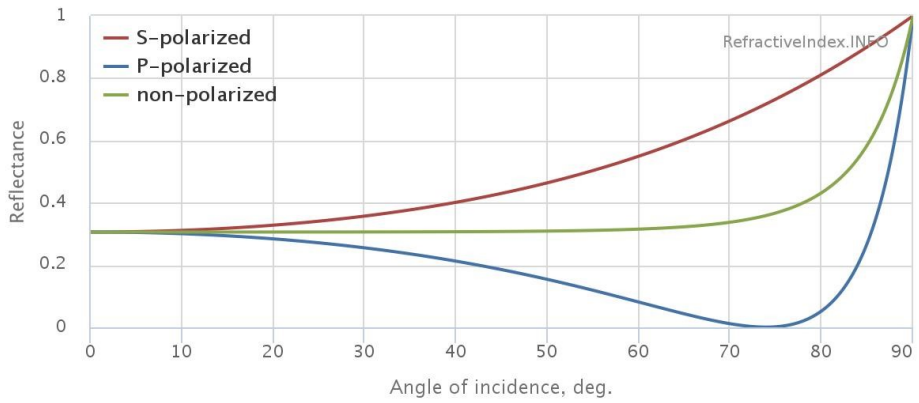

Figure 46: Reflectance of InP (at wavelength of 800nm) as function of incidence angle for s-polarized (red), p-polarized (blue) and non-polarized (green) light. (Original figure [38])

The planarizing filling material between the nanowires in the main NWSC could affect the effective refractive index of the cell. The refractive index of this material (benzocyclobutene) is approximately 1.54 which is considerably lower than the value for InP. Hence one could expect to find a shifted Brewster angle (if existing) for the NWSC compared to that of pure and planar InP.

Simulation

Nicklas Anttu so kindly provided a simulation of the angular dependence for different polarizations. The model of the InP solar cell model used the geometric parameters given in Figure 47. The figure also demonstrates the definition of the two polarizations and the angle θ. The nanowires where modelled in a hexagonal pattern with a spacing of 500 nm corresponding to the actual design of the experimentally tested NWSC.

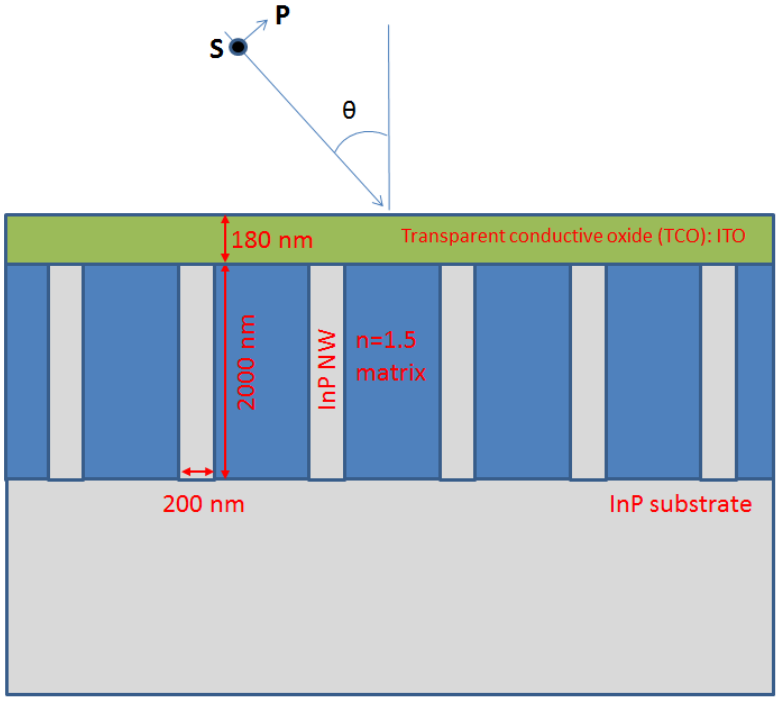

Figure 47: Shows the simulated NWSC with attributed parameters and definition of angle and polarization direction.

In the simulation the absorptance of the nanowires is modelled. This is defined as the number of photons incident on the sample that is absorbed, i.e. the absorptance does not change according to the cosine law as the incidence angle is changed. The experimental data will be given in photocurrent intensity as instead of absorption. The absorptance simply gives the probability for a photon to be absorbed in the nanowire. The photocurrent on the other hand is also dependent on the probability of a photo generated charge carrier to be collected, something that is influenced by several different properties within the wire. Experimental data may hence deviate from the simulation results but the simulations should be a good indication as to what is expected from the experimental data. Simulation results are shown in Figure 48. The low absorptance seen for 300 nm is due to high absorption in the ITO at that energy.

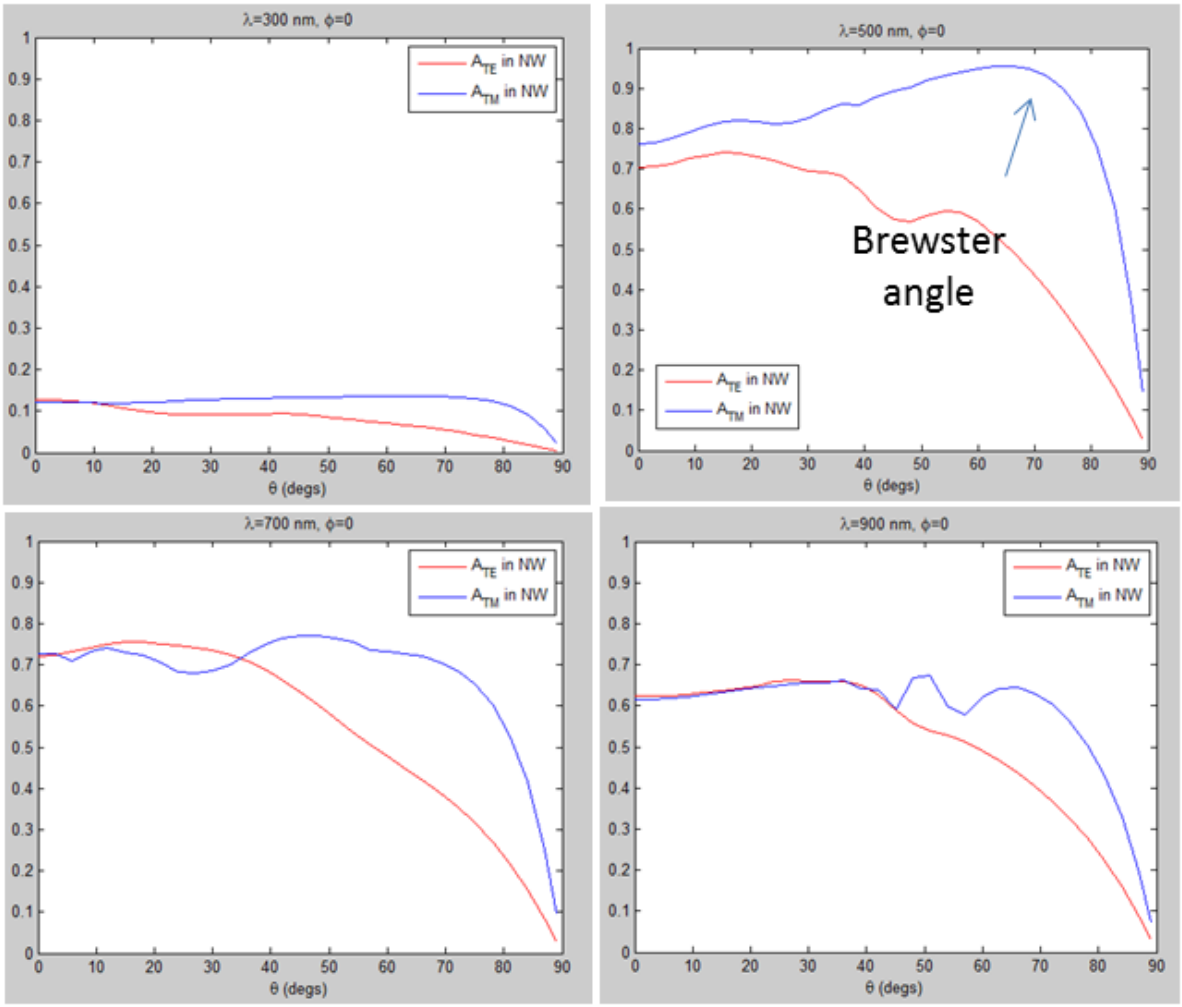

Figure 48: Results from the simulation showing the absorptance in the nanowires as function of angle for wavelength of 300nm (top left), 500nm (top right), 700nm (bottom left) and 900nm (bottom right). Red and blue lines indicate s and p polarized light respectively.

6.2. Measurement Setup

The polarization dependence was measured using the same procedure as for the angular dependence, the only difference being that they were made for S and P polarizations respectively.

This experiment required a linear polarizer to be added to the angular dependence setup, placed between the light source and the sample. The spectral performance of the polarizer was tested using a second polarizer. These were placed in front of each other with crossed, orthogonal linear polarizations. For wavelengths where the polarizer actually polarizes the light the intensity should be well below the nonpolarized intensity. The two polarizers should be blocking the light at these wavelengths. The result of the test is shown in Figure 49. For energies above 1.5 eV (~830 nm) the polarizer works effectively. For lower energies the polarization strongly decreases which should be kept in mind when looking at the polarization dependence at such energies.

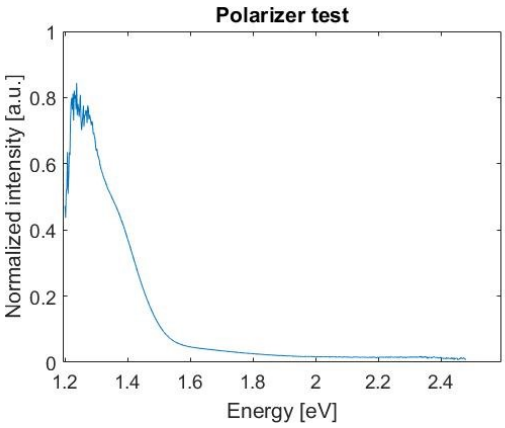

Figure 49: Ratio of induced current as the incident light passes through orthogonally crossed polarizers to the current for nonpolarized light. The polarizers work well for energies above 1.5eV where more than 90% of the light is polarized.

6.3. Results and Discussion

The measurement data was plotted in correspondence to the simulated information given in the Theory (Figure 48). Plots for 300 nm are not possible to present due to the low light source intensity at this wavelength.

The intensity for P and S polarization was normalized to the cosine law and plotted as function of angle for 500 nm, 600 nm, 700 nm and 900 nm in Figure 50.

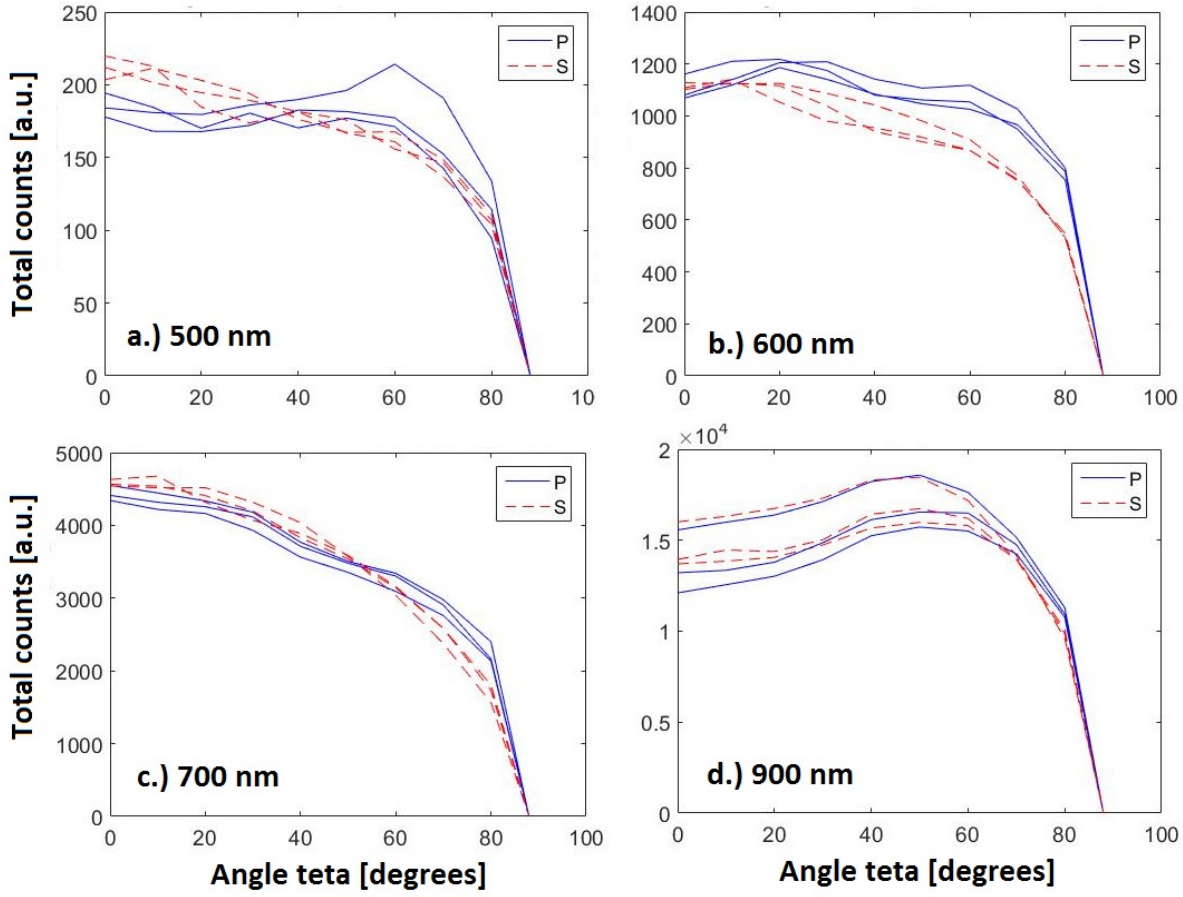

Figure 50: Current intensity for S and P polarization (red and blue line respectively) as function of angle. Three devices were measured corresponding to the three lines of every polarizatrion in every plot. Values at a.) 500 nm, b.) 600 nm, c.) 700 nm and d.) 900 nm.

Comparing these result with the simulation the real NWSC shows the same polarization-angular dependence but weaker. The Brewster angle, which the simulation indicated to be 60°, is not obvious in these results. For 600 nm there is a maximum difference between S and P polarization for angles between 65° and 80°. At 700 nm this difference seems to be maximized at 80° while it (especially for one device) seems to be at 60° for the 500 nm plot. For wavelengths above 830 nm (1.5 eV) the polarizer doesn't work effectively (acc. to Figure 49) and this can be seen in Figure 50 where the S and P polarizations aren't significantly differing from one another.

In Figure 24 it is seen that device J shows higher angular dependence than D. During the data analysis it is also noticed that the polarization dependence is higher for device J than D. Can these differences be related to the fact that J has surface artifacts covering large areas while D does not? It is known that surface roughness decreases reflection ([43]), which would in this case explain the relative increase in photocurrent with increasing angle for device J compared to D (and other devices). A future investigation on how to optimize the surface morphology could be relevant for optimizing of the NWSC to actual operating conditions.

7. Conclusions and Outlook

SPCM

The SPCM setup developed achieved a resolution of 0.55-1 µm. The reflection detection was a great addition to the setup as complement to the PCI. Analyzing the results from the PCIs and RIs together gave information about the defects that could help determining how grave their impact on the performance was.

The overall performance of the devices was very good showing high quality NWSCs. The defects that were found were distinguished by different characteristics. A typical defect showing missing NW shows up as a point with low current and high reflectivity. Defects with both high reflectivity and high photocurrent are evidence of artifacts with intact NWs but imperfections in covering layers. Scratches with broken/badly contacted NW show low reflectivity *and* low current.

The PCI and RI information provided may also indicate the origin of the defects and that way provide information of how to avoid them. Artifact in Figure 28, artifact 1, seems to originate from a liquid that has run along the device. This could be the BCB which is deposited in liquid form. When it comes to spots of missing nanowires these are likely to originating from the NW growth itself where gold particles have been missing or badly attached. This is motivated by the fact that defects at that scale are unlikely to be caused by exterior damaging effects. Defects that seem to only affect the reflectance are believed to originate from substrates around the NW. The type of defect seen in defect 2 in Figure 23 is likely a dirt particle that has been attached to the surface after deposition of the surface layers.

These are speculations about the defect origins that further characterization, such as SEM, could give more information about. It may be concluded that the PCI and RI technique gives important information about defects, their impact on the photocurrent and possible origin, but the information needs to be compared to complementing morphology information (or similar) in order to establish origin and hence how to avoid them.

Another defect characteristic is the magnitude of their impact, generally the large defects gave a lower current decrease than point defects or defects on NW scale. Nonetheless both type of defects showed to affect the total device current similarly and to improve NWSC performance they should both be diminished.

The scanning technique indicated factors that could be further improved such as reflection saturation, quantitative reflection detection and start blur. In order to gain further information about the device and the SPCM technique a laser of different wavelength would be interesting to use. A longer laser wavelength would presumably show higher contrasts for nanowire gaps and surface roughness as is indicated in Figure 9 [24]. A longer wavelength could that way improve the resolution, while still a trade off has to be made since it will result in larger spotsize.

Angular and polarization dependence

Automating the angular dependence measurement would be convenient and may increase accuracy and reliability. As for the results obtained the angular dependence for the NWSCs showed to follow the dependence of planar devices for the full spectrum. Looking at the angular dependence for different energies other behaviors were found. These can be attributed to the nanowire structure

interacting with the radiation. This behavior in relation to implementing the solar cells on static racks or using solar concentrators may be an interesting subject for future investigation.

The interesting part was to look into how the angular dependence and defects were correlated. Device J showed the strongest angular dependence together with the largest surface defect which is unlikely to be a coincidence. Knowing the normal (ideal) angular dependence for a certain device design could open up for a new way of analyzing the NWSC. That information could be used as reference to check for defects and surface roughness of new devices of the same design. It may also be used in order to optimize the surface morphology for highest possible absorption for relevant angle. This could be an interesting subject for future investigation. For such an investigation multiple measurements on similar devices would be needed to determine the angular dependence for that particular geometry.

To say more about the angular dependence and its origin it would be interesting to measure a device without the planarizing BCB layer. It could also be interesting to use a light source with higher intensity at high energies. The NWSC is believed to generate photocurrent up to 300 nm where it sharply decreases due to increased absorption in the ITO.

The polarization of the incoming light did not have a large influence on the induced photocurrent and its angular dependence. Information about the polarization dependence would therefor presumably be important for understanding the NWSC performance but not as a parameter to take into account for optimizing the design. For further investigations it would be interesting to use a polarizer that works effectively also at low energies and a light source with higher intensity at high energies.

The different measurement setups have shown to give information that characterizes the NWSC and opened up for several aspects to be further investigated. Establishing ways of improving the NWSC design and to minimize defects turned out to be complex for already well optimized NWSCs. However developing the work done in this Thesis, by means suggested, could indeed lead to such improvements.

Bibliography

[1] A. Neslen, "Record boost in new solar power continues massive industry growth," the guardian, 9 June 2015. [Online]. Available: http://www.theguardian.com/environment/2015/jun/09/record-boost-in-new-solar-power-continues-massive-industry-growth. [Accessed 16 January 2016].

[2] M. A. Green, K. Emery, Y. Hishikawa, W. Warta and E. D. Dunlop, "Solar cell efficiency tables (version 47)," *Progress in Photovoltaics: Research and Applications,* pp. 3-11, 2016.

[3] K. Masuko, D. Fujishima, M. Shigematsu, T. Hashiguchi and M. Kai, "Achievement of More Than 25% Conversion Efficiency With Crystalline Silicon Heterojunction Solar Cell," *IEEE Journal of Photovoltaics,* vol. 4, no. 6, pp. 1433 - 1435, 2014.

[4] M. A. Maehlum, "Which Solar Panel Type is Best? Mono- vs. Polycrystalline vs. Thin Film," ENERGY INFORMATIVE, THE HOMEOWNER`S GUIDE TO SOLAR PANELS, 18 May 2015. [Online]. Available: http://energyinformative.org/best-solar-panel-monocrystalline-polycrystalline-thin-film/#crystalline-silicon. [Accessed 9 March 2016].

[5] H. Q. W. Shockley, "Detailed Balance Limit of Efficiency of p-n Junction Solar Cells," *Journal of Applied Physics,* vol. 32, p. 510, 1961.

[6] M. T. Borgström, J. Wallentin, M. Heurlin, S. Fält, P. Wickert, J. Leene, H. M. Magnusson, K. Deppert and L. Samuelson, "Nanowire swith promise for Photovoltaics," *IEEE Journal of Selected Topics in Quantum Electronics,* vol. 17, no. 4, pp. 1050-1061, 2010.

[7] K. W. Böer, "Chemistry Explained, Foundations and applications," Advameg, Inc., 2016. [Online]. Available: http://www.chemistryexplained.com/Ru-Sp/Solar-Cells.html.

[8] S. M. Sze and M.-K. Lee, Semiconductor devices, Physics and Technology, Singapore: Wiley, 2012.

[9] R. Nave, "Forward Biased P-N Junction," HyperPhysics, Department of Physics and Astronomy, Georgia State University, [Online]. Available: http://hyperphysics.phy-astr.gsu.edu/hbase/solids/diod.html. [Accessed 12 February 2016].

[10] M. Britt, "Pn junction equilibrium," Wikipedia Commons, 8 September 2006. [Online]. Available: https://commons.wikimedia.org/wiki/File:Pn_junction_equilibrium.svg. [Accessed 9 February 2016].

[11] "UC Davis SolarWiki, 2. Illuminated Characteristics," University of California, [Online]. Available: http://solarwiki.ucdavis.edu/The_Science_of_Solar/Solar_Basics/D._P-N_Junction_Diodes/IV._Behaviors_of_the_p-n_Junction/2._Illuminated_Characteristics. [Accessed 10 April 2016].

[12] ENERGY.GOV, "Photovoltaic Cell Quantum Efficiency Basics," ENERGY.GOV, Office of energy & renewable energy, 20 August 2013. [Online]. Available: http://energy.gov/eere/energybasics/articles/photovoltaic-cell-quantum-efficiency-basics. [Accessed 16 January 2016].

[13] C. Honsberg and S. Bowden, "Quantum Efficiency," Photovoltaics Education Network, PV Education, [Online]. Available: http://www.pveducation.org/pvcdrom/pn-junction/introduction. [Accessed 12 February 2016].

[14] C. Honsberg and S. Bowden, "The photovoltaic effect," The Photovoltaic Education Network, PV Education, [Online]. Available: http://www.pveducation.org/pvcdrom/solar-cell-operation/photovoltaic-effect. [Accessed 12 February 2016].

[15] J. Kupec, R. L. Stoop and B. Witzigmann, "Light absorption and emission in nanowire array solar cells," *Optics Express,* vol. 18, no. 26, pp. 27589-27605, 2010.

[16] C. Honsberg and S. Bowden, "Open-Circuit Voltage," The Photovoltaic Education Network, PV Education, [Online]. Available: http://www.pveducation.org/pvcdrom/solar-cell-operation/open-circuit-voltage. [Accessed 20 February 2016].

[17] C. Honsberg and S. Bowden, "Efficiency," The Photovoltaic Education Network, PV Education, [Online]. Available: http://www.pveducation.org/pvcdrom/solar-cell-operation/efficiency. [Accessed 20 February 2016].

[18] H. Joyce, Q. Gao, H. Tan and C. Jagadish, "Process to grow nanowires controls key properties," *SPIE Newsroom,* p. 1776, 9 Spetember 2009.

[19] P. Peter Krogstrup, H. Ingerslev Jørgensen, M. Heiss, O. Demichel, J. V. V. Holm, M. Aagesen, J. Nygard and A. Fontcuberta i Morral, "Single-nanowire solar cells beyond the Shockley–Queisser limit," *Nature Photonics,* vol. 7 , no. 1038, p. 306–310, 2013.

[20] E. Garnett and P. Yang, "Light Trapping in Silicon Nanowire Solar Cells," *Nano Letters,* vol. 10, no. 1021, pp. 1082-1087, 2010.

[21] J. Wallentin, N. Anttu, A. Asoli, M. Huffman, I. Åberg, M. H. Magnusson2, G. Siefer, P. Fuss-Kailuweit, F. Dimroth, B. Witzigmann, H. Xu, L. Samuelson, K. Deppert and M. T. Borgström, "InP Nanowire Array Solar Cells Achieving 13.8% Efficiency by Exceeding the Ray Optics Limit," *Science,* vol. 339, no. 6123, pp. 1057-1060, 2013.

[22] J. Wallentin and M. T. Borgström, "Doping of semiconductor nanowires," *Journal of Materials Research,* vol. 26, no. 17, pp. 2142-2156, 2011.

[23] M. Burghard and A. Mews, "High-Resolution Photocurrent Mapping of Carbon Nanostructures," *ACS Nano,* vol. 6, no. 7, p. 5752–5756, 2012.

[24] S. L. Howell, S. Padalkar, K. Yoon, Q. Li, D. D. Koleske, J. J. Wierer, G. T. Wang and L. J. Lauhon, "Spatial Mapping of Efficiency of GaN/InGaN Nanowire Array Solar Cells Using Scanning Photocurrent Microscopy," *Nano Letters,* vol. 13, no. 11, p. 5123–5128, 2013.

[25] A. Lysov, S. Vinaji, M. Offer, C. Gutsche, I. Regolin, W. Mertin, M. Geller, W. Prost, G. Bacher and F.-J. Tegude, "Spatially resolved photoelectric performance of axial GaAs nanowire pn-diodes," *Nano Research,* vol. 4, no. 10, pp. 987-995, 2011.

[26] G. Jacobs, "Understanding of Spot Size for Laser Scanning," Professional Surveyor magazine, 2006.

[27] M. C. Putnam, S. W. Boettcher, M. D. Kelzenberg, D. B. Turner-Evans, J. M. Spurgeon, E. L. Warren, R. M. Briggs, N. S. Lewis and H. A. Atwater, "Si microwire-array solar cells," *Energy & Environmental Science,* vol. 3, no. 8, pp. 1037-1041, 2010.

[28] G. Mariani, P.-S. Wong, A. M. Katzenmeyer, F. Léonard, J. Shapiro and D. L. Huffaker, "Patterned Radial GaAs Nanopillar Solar Cells," *Nano Letters,* vol. 11, no. 6, pp. 2490-2494, 2011.

[29] M. C. T. Bahaa E. A. Saleh, Fundamentals of Photonics, 2nd Edition, New York: Wiley, 2007.

[30] Sintec Optronics Pte Ltd, "Focused Beam Diameter with Focusing Lens," [Online]. Available: www.sintecoptronics.com . [Accessed 30 April 2016].

[31] Stanford Research Systems, "About Lock-In Amplifiers," [Online]. Available: http://www.thinksrs.com/. [Accessed 12 February 2016].

[32] K. Jack, "VIDEO BASICS," Nuts and Volts, January 2005. [Online]. Available: http://www.nutsvolts.com/magazine/article/video_basics. [Accessed 30 May 2016].

[33] Sol Voltaics , *EA012 Etestlog,* Lund.

[34] G. Seibert, "Solar cell output as Function of Angle of Incidence for both unpolarized and Linear Polarized Light," *Science Direct,* vol. 8, pp. 121-123, 1968.

[35] J. Zhu, Z. Yu, G. F. Burkhard, C.-M. Hsu, S. T. Connor, Y. Xu, Q. Wang, M. McGehee, S. Fan and Y. Cui, "Optical Absorption Enhancement in Amorphous Silicon Nanowire and Nanocone Arrays," *Nano Letters,* vol. 9, no. 1, pp. 279-282, 2009.

[36] Y. Li, M.-Y. Lee, H.-W. Cheng and Z.-L. Lu, "3D simulation of morphological effect on reflectance of Si3N4 sub-wavelength structures for silicon solar cells," *Nanoscale Research Letters,* vol. 7, no. 1, p. 196, 2012.

[37] M. Polyanskiy, "Refractive index database, Optical constants of Si3N4 (Silicon nitride)," RefractiveIndex.INFO , 2008-2016. [Online]. Available: http://refractiveindex.info/?shelf=main&book=Si3N4&page=Philipp. [Accessed 28 April 2016].

[38] M. Polyanskiy, "Refractive index database, Optical constants of InP (Indium phosphide)," RefractiveIndex.INFO , 2008-2016. [Online]. Available: http://refractiveindex.info/?shelf=main&book=InP&page=Aspnes. [Accessed 28 April 2016].

[39] E. W. Weisstein, "Fourier Transform Spectrometer," Wolfram Research, 1996-2007. [Online]. Available: http://scienceworld.wolfram.com/physics/FourierTransformSpectrometer.html. [Accessed 23 February 2016].

[40] R. Nave, "Polarization by Reflection," Hyperphysics, DEpartment of Physics and Astronomy, Georgia State University, [Online]. Available: http://hyperphysics.phy-astr.gsu.edu/hbase/phyopt/polref.html. [Accessed 25 April 2016].

[41] M. C. Fink, "The Polarization of Light by Reflection," Omega Optical Inc., 2008. [Online]. Available: http://www.photonics.com/Article.aspx?AID=35808. [Accessed 25 April 2016].

[42] D. R. Paschotta, "Refraction," RP Photonics, [Online]. Available: https://www.rp-photonics.com/refraction.html. [Accessed 25 April 2016].

[43] A. A. Maradudin and D. L. Mills, "Scattering and absorption of electromagnetic radiation by a semi-infinite medium in the presence of surface roughness," *Physical Review B,* vol. 11, p. 1392 , 1975.

[44] Y. H. Ahn, A. Tsen, B. Kim, Y. W. Park and J. Park, "Photocurrent Imaging of p−n Junctions in Ambipolar Carbon Nanotube Transistors," *Nano Letters,* vol. 7, no. 11, pp. 3320-3323, 2007.

[45] B. Curtin, *Spatially resolved Photocurrent mapping of nanowire array solar cells for analysis of factors affecting cell efficiency,* Lund: LUP Student Papers , 2012.

[46] Melles Griot, *Nanomover II, Operator's Manual,* Mercer Island: Applied Precicion, Inc., 1995.